

On the gas content of transitional disks: a VLT/X-Shooter study of accretion and winds[★]

C. F. Manara¹, L. Testi^{1,2,3}, A. Natta^{2,4}, G. Rosotti^{5,6}, M. Benisty⁷, B. Ercolano^{5,3}, L. Ricci⁸

¹ European Southern Observatory, Karl Schwarzschild Str. 2, 85748 Garching, Germany
e-mail: cmanara@eso.org

² INAF - Osservatorio Astrofisico di Arcetri, Largo E.Fermi 5, I-50125 Firenze, Italy

³ Excellence Cluster Universe, Boltzmannstr. 2, D-85748 Garching bei München, Germany

⁴ School of Cosmic Physics, Dublin Institute for Advanced Studies, 31 Fitzwilliam Place, Dublin 2, Ireland

⁵ Universitäts-Sternwarte München, Scheinerstr. 1, 81679 München, Germany

⁶ Max Planck Institut für Extraterrestrische Physik, Giessenbachstrasse 1, 85748 Garching bei München, Germany

⁷ Institut de Planétologie et Astrophysique Grenoble, 414 rue de la Piscine, 38400 St-Martin d'Hères, France

⁸ California Institute of Technology, 1200 East California Boulevard, 91125 Pasadena, CA, USA

Received December 22, 2013; accepted June 4, 2014

ABSTRACT

Context. Transitional disks are thought to be a late evolutionary stage of protoplanetary disks whose inner regions have been depleted of dust. The mechanism responsible for this depletion is still under debate. To constrain the various models it is mandatory to have a good understanding of the properties of the gas content in the inner part of the disk.

Aims. Using X-Shooter broad band - UV to NIR - medium resolution spectroscopy we derive the stellar, accretion, and wind properties of a sample of 22 transitional disks. The analysis of these properties allows us to put strong constraints on the gas content in a region very close to the star ($\lesssim 0.2$ AU) which is not accessible with any other observational technique.

Methods. We fit the spectra with a self-consistent procedure to derive simultaneously spectral type, extinction, and accretion properties of the targets. From the continuum excess at near-infrared wavelength we distinguish whether our targets have dust free inner holes. Analyzing forbidden emission lines we derive the wind properties of the targets. We then compare our findings to results for classical T Tauri stars.

Results. The accretion rates and wind properties of 80% of the transitional disks in our sample, which is strongly biased towards strongly accreting objects, are comparable to those of classical T Tauri stars. Thus, there are (at least) some transitional disks with accretion properties compatible with those of classical T Tauri stars, irrespective of the size of the dust inner hole. Only in 2 cases the mass accretion rates are much lower, while the wind properties remain similar. We do not see any strong trend of the mass accretion rates with the size of the dust depleted cavity, nor with the presence of a dusty optically thick disk very close to the star. These results suggest that, close to the central star, there is a gas rich inner disk with density similar to that of classical T Tauri stars disks.

Conclusions. The sample analyzed here suggests that, at least for some objects, the process responsible of the inner disk clearing should allow for a transfer of gas from the outer disk to the inner region. This should proceed at a rate that does not depend on the physical mechanism producing the gap seen in the dust emission and results in a gas density in the inner disk similar to that of unperturbed disks around stars of similar mass.

Key words. Stars: pre-main sequence – stars: formation – protoplanetary disks – accretion, accretion disks

1. Introduction

At the beginning of their evolution, protoplanetary disks surrounding forming stars appear as a continuous distribution of gas and small dust particles. For the first few Myrs they evolve by viscous accretion (Hartmann et al., 1998), and in the meantime grain growth and planet formation take place. The observations show that, in a relatively small fraction of objects ($\sim 10\%$, e.g., Espaillat et al. 2014), a significant change in the disk morphology is detected: a dust-depleted region in the inner part of the disk appears in mm-interferometry observations (e.g. Andrews et al., 2011) and/or as a dip in the mid-IR spectral energy distribution (SED; e.g., Merín et al., 2010). This can be either a

hole - absence of gas from the dust sublimation radius out to some much larger radius - or a *gap* - absence of gas in a relatively narrow region, like a ring. These disks are known as transitional disks (TDs; e.g., Calvet et al., 2005; Espaillat et al., 2014). In some cases an excess emission is detected at near-infrared wavelengths; this emission comes from a small annulus of warm dust close to the star (e.g., Benisty et al., 2010). These objects are commonly referred to as pre-transitional disks (PTDs; e.g., Espaillat et al., 2010, 2014).

Different processes have been proposed to explain the formation of these gaps/holes. The most plausible mechanisms so far are photoevaporation, grain growth, or planet formation (e.g., Espaillat et al., 2014). Still, none of these processes alone has been shown to be sufficient to explain all observations. Grain growth models explain the observed IR SEDs of TDs, but are unable to reproduce mm-observations (Birnstiel et al., 2012). The detection of large mass accretion rates (\dot{M}_{acc}) in several TDs with large inner hole sizes is at odds with photoevaporative model

[★] This work is based on observations made with ESO Telescopes at the La Silla Paranal Observatory under programme ID 089.C-0840 and 090.C-0050, and on data obtained from the ESO Science Archive Facility observed under programme ID 084.C-1095, 085.C-0764, 085.C-0876, 288.C-5013, and 089.C-0143.

predictions, which expect a very fast depletion of the gas mass reservoir for accretion by the inner disk onto the star (e.g. Owen et al., 2011, 2012). Moreover, planet formation models, which need to include multiple accreting planets to perturb sufficiently the inner disk surface density, still cannot explain TDs with large inner hole sizes and high mass accretion rates (Zhu et al., 2011). At the same time, the presence of a planet could explain the radial and azimuthal distribution of mm-sized grain particles in TDs (Pinilla et al., 2012). New attempts are being made to include various processes in one model. As an example, Rosotti et al. (2013) combined photoevaporation and planet formation, but they were still not able to explain the observed accretion properties of many TDs. Similar constraints arise from observations of winds in TDs. Analysis of forbidden line emission show that winds are emitted from the innermost region of the disk in various objects (Alexander et al., 2014), and these observations suggest that photoevaporation could play a role in the clearing of disks. At the same time, it is not yet clear what is the origin and what are the properties of these winds, and more studies are needed to have a clearer understanding of this aspect.

In this context, the combination of inner hole size, \dot{M}_{acc} , and wind properties is a powerful observational diagnostic of disk evolution models. In particular, \dot{M}_{acc} and the wind properties allow us to place strong constraint on the gaseous content of the innermost region of these disks which can be compared with the models. As explained by magnetospheric accretion models (e.g. Hartmann et al., 1998), the process of accretion is related to the gaseous content of the innermost region of the disk at radii $\lesssim 0.2$ AU. Similarly, forbidden lines are emitted in regions in the disk as close as ~ 0.2 AU from the central star. The measurements of \dot{M}_{acc} for TDs available in the literature are mostly based on secondary indicators (such as the 10% H α width) and have been obtained using different non-homogeneous techniques. In many cases these values are highly uncertain and, therefore, not reliable. At the same time, very few data on the wind properties for TDs are available. In order to remedy these deficiencies we have collected a sample of 22 spectra of TDs with the ESO VLT/X-Shooter spectrograph. We aim at deriving with an highly reliable method the stellar and accretion properties of these objects and to study simultaneously their wind properties from optical forbidden lines.

The analysis of this sample of TDs that we present here is focused firstly on deriving the values of \dot{M}_{acc} for these objects in order to verify the reliability of those reported in the literature. We use a very detailed and self-consistent analysis to derive accretion rates and simultaneously the spectral types and stellar properties of the objects from the fit of the whole spectrum from UV to NIR. In particular, we want to check the high values of \dot{M}_{acc} for objects with large inner hole sizes, that cannot be explained by current models. At the same time, we want to determine whether there is any dependence of the accretion properties of TDs with their disk morphology, in particular testing possible correlation with the inner hole size. Moreover, we investigate the differences and similarities in accretion and wind properties of TDs with respect to classical T Tauri stars. Finally, we put constraint on the properties of the gaseous innermost regions of the disk in these objects from the derived values of \dot{M}_{acc} and from the wind properties.

The paper is organized as follows. In Sect. 2 we present the observations, the data reduction procedure, and the properties of the targets in our sample. In Sect. 3 we briefly describe the method used to derive the stellar and accretion properties of the objects, and we report the derived values. Then, in Sect. 4 we derive the wind properties of our targets. In Sect. 5 we discuss our

results and describe the additional data from the literature collected to derive our conclusions, which we summarize in Sect. 6.

2. Observations

All the observations included in this work have been obtained with the ESO/VLT X-Shooter spectrograph. This medium resolution and high-sensitivity instrument covers simultaneously the wavelength range between ~ 300 nm and ~ 2500 nm, dividing the spectrum in three arms, namely the UVB arm in the region $\lambda \sim 300\text{--}560$ nm, the VIS arm between $\lambda \sim 560\text{--}1020$ nm, and the NIR arm from $\lambda \sim 1020$ nm to $\lambda \sim 2500$ nm (Vernet et al., 2011). In the following, we present the properties of the sample, the details of the observations, that are reported also in Table 1-2, and the data reduction procedure.

2.1. Sample description

The first criterion used to select the objects in our sample was to include all the targets with known inner hole sizes (R_{in}) larger than ~ 20 AU and large \dot{M}_{acc} ($\gtrsim 10^{-9} M_{\odot}/\text{yr}$). These were selected mainly from the sample of Andrews et al. (2011), where the value of R_{in} has been measured using resolved mm-interferometry observations. From this sample we selected the 8 objects with spectral type later than G2. For two of these objects (LkCa15, ISO-Oph 196) the X-Shooter spectra were available in the ESO archive, while we observed the remaining six targets (LkH α 330, DM Tau, GM Aur, RX J1615-3255, SR21, and DoAr 44) during our programs (see Table 1). We added to these objects also four TDs for which R_{in} was derived from IR SED fitting by Merín et al. (2010) and Kim et al. (2009), namely SZ Cha, CS Cha, Sz 84, and Ser 34. Only for the latter the spectrum was not available in the ESO archive.

Then, we included some objects with smaller inner hole sizes and different values of \dot{M}_{acc} , both as high as the object with large R_{in} and smaller than those. In particular, we included five targets whose spectra were not available in the ESO archive and with $R_{\text{in}} \leq 15$ AU and as small as 1 AU, namely Oph22, Oph24, and Ser29 from the sample of Merín et al. (2010), RX J1842.9 and RX J1852.3 from Hughes et al. (2010). Finally, we collected all the spectra of TDs classified by Kim et al. (2009) available in the ESO archive (four objects, CHXR22E, Sz 18, Sz 27, and Sz 45) and the spectrum of TWHya, whose R_{in} has been measured with resolved mm-observations by Hughes et al. (2007). In total the sample analyzed here comprises 22 objects.

For 9 of the objects analyzed here the value of R_{in} has been directly determined from resolved mm-interferometry observations (Hughes et al., 2007; Andrews et al., 2011), while for the remaining 13 targets the classification as TD and the size of the inner hole has been determined from IR SED fitting (Kim et al., 2009; Merín et al., 2010; Hughes et al., 2010; Espaillat et al., 2013). The list of targets, their distances, and the values of R_{in} available in the literature are reported in the first three columns of Table 3. The objects are located in different star forming regions (Perseus, Taurus, Chameleon, TW Hydrae, Lupus, ρ -Ophiucus, Serpens, Corona Australis) and have values of R_{in} between ~ 1 to ~ 70 AU, being representative of the whole range of measured values of R_{in} . When both values of R_{in} obtained using IR SED fitting and mm-interferometry resolved observations are available we adopt in the analysis the mm-interferometry result. More information on individual objects in the sample are reported in Appendix A.1.

Even if the sample is containing objects of different TD morphologies, such as various inner hole sizes, this is not statisti-

cally complete and it is in general biased toward accreting TDs. As explained before, our selection criteria were aimed at observing TDs with already known and high accretion rates, thus our own observations represent a biased sample. On the other hand, the targets collected in the literature were in some cases selected with different criteria that could mitigate our biases. Unfortunately, it is not possible to estimate completely the bias in its selection.

2.1.1. Class III properties

Here we present the properties of three non-accreting (Class III) YSOs, that we use as photospheric templates in our analysis (see Sect. 3) to enlarge the available sample of Class III YSOs observed with X-Shooter and presented in Manara et al. (2013a). We follow the same procedure as in Manara et al. (2013a) to derive their spectral types and stellar properties, which are reported in Table 2.

The YSO IC348-127 has spectral type (SpT) G4 (Luhman et al., 1998, 2003) and has been classified as Class III from Lada et al. (2006) using Spitzer photometry. This classification, with values of extinction $A_V \sim 6$ mag, has been confirmed by Cieza et al. (2007) and Dahm (2008). We confirm the spectral classification and the extinction, and we derive $L_* = 12.9 \pm 5.9 L_\odot$ for this object. Due to the very high A_V , the spectrum of this target at $\lambda \lesssim 350$ nm is very noisy.

The second Class III YSO included in this work is T21, which has been classified as a Class III YSO with SpT G5 by Manoj et al. (2011, and references therein). The typical reddening law of the Chameleon I region in which this object is located is not well constrained (Luhman, 2008), and could be described using values of R_V (Cardelli et al., 1989) up to 5.5. By comparison of the dereddened spectrum with a blackbody at $T=5770$ K, which is the typical T_{eff} of a star with SpT G5, we obtain that the extinction towards this object is better represented using $R_V = 3.1$ and $A_V = 3.2$ mag. Adopting these values, the derived luminosity of the target is $L_* = 18.5 \pm 8.5 L_\odot$.

Finally, we include in the sample CrA75, which has been classified as a Class III YSO with SpT K2 from Forbrich & Preibisch (2007, and references therein). This has been later confirmed by Peterson et al. (2011) and Currie & Sicilia-Aguilar (2011), who suggested that the correct values of extinction for this object is $A_V=1.5$, assuming $R_V=5.5$, representative of objects in the Corona Australis region (Peterson et al., 2011; Chapman et al., 2009). With these parameters we derive for CrA75 $L_* = 0.4 \pm 0.2 L_\odot$.

The objects whose properties have been described in this section expand the coverage in SpT of our library of photospheric template. This, however, remains incomplete. In particular, the objects presented in Manara et al. (2013a) have an almost uniform coverage in the SpT range from K5 to M6.5. The three objects presented here, instead, do not cover entirely the range of SpT from G3 to K5. This incompleteness of photospheric templates in this range will be considered in the analysis.

2.2. Observational strategy

As explained before, we have included in the analysis both new observations and archival data. In the following, we describe separately our observational strategy and the settings used in the archival observations.

2.2.1. New observations

New observations with the ESO/VLT X-Shooter spectrograph have been carried out in service mode between April and November 2012 (ESO Pr.Id. 089.C-0840 and 090.0050, PI Manara). The targets have been observed in ABBA slit-nodding mode to achieve the best possible sky subtraction also in the NIR arm. The objects have been observed using different slit widths in the UVB arm. For the brightest objects the slit $0.5 \times 11''$, which leads to the highest spectral resolution in this arm ($R=9100$), has been adopted, while for the fainter objects - namely Oph22, Oph24, Ser29, and Ser34 - we have used the $1.0 \times 11''$ slit, which leads to a lower resolution ($R=5100$) but allows to achieve an higher S/N. In the VIS and NIR arms the $0.4 \times 11''$ slit has been adopted for all the targets. This slit width leads to the highest possible resolution ($R=17400$, 10500 in the VIS and NIR arms, respectively) and to enough S/N in the spectra. The read-out mode used was in all cases “100,1x1,hg”. To obtain a better flux calibration, we observed the targets of Pr.Id. 090.0050 with the large slit ($5.0 \times 11''$) immediately after the exposure with the narrow slit. With the large slit we obtain spectra with a lower resolution but, at the same time, we avoid slit losses and we get a reliable flux calibration for this spectrum, which is then used to calibrate the narrow slit one (see Sect. 2.3). The names of the targets, their coordinates, observing date, and exposure times of the observations are summarized in Table 1.

We observed in our programs also two Class III YSOs (see Sect. 2.1.1 for details). We observed CrA 75 using the narrower slits in each arm - $0.5 \times 11''$ in the UVB arm, $0.4 \times 11''$ in the VIS and NIR arms - to obtain the highest possible spectral resolution. For IC348-127, we adopted the slit widths $1.6 \times 11''$, $1.5 \times 11''$, and $1.2 \times 11''$ in the UVB, VIS, and NIR arms, respectively. This was done in order to achieve enough S/N in the available observing time. We recap in Table 2 these information.

2.2.2. Archival data

The data included in our analysis collected from the ESO archive have been obtained using different observational strategies. The observational data are presented here and summarized in Table 1 and 2.

The transitional disk Sz 84 has been observed during the INAF GTO time in Pr.Id. 089.C-0143 (PI Alcalá). The adopted slits width for this object were $1.0 \times 11''$ in the UVB arm and $0.9 \times 11''$ in the VIS and NIR arms. More details on the observing procedure and on the data reduction for this targets are given in Alcalá et al. (2014).

The target ISO-Oph 196 was observed for the program Pr.Id. 085.C-0876 (PI Testi) using the same settings as the one adopted in our observations. We include in our analysis two targets - namely DoAr44 and TW Hya - from the program Pr.Id. 085.C-0764 (PI Guenther). Both targets have been observed with the narrow slits. For all these observations the readout mode used was “100,1x1,hg”, as in our programs, and for each object 4 exposures in the ABBA slit-nodding mode were taken.

We consider in our work also seven objects from the program Pr.Id. 084.C-1095 (PI Herczeg). Six of those - namely CS Cha, CHXR22E, Sz18, Sz27, Sz45, and Sz Cha - are TDs, while T21 is a Class III YSOs. These targets have been observed both with a narrow-slit setting (slit widths $1.0 \times 11''$ in the UVB and $0.4 \times 11''$ in the VIS and NIR arms) and with the large slit to have a better flux calibration of the spectra. The narrow-slit observations have been carried out with the “400,1x2,lg” mode with a

AB slit-nodding mode. The large-slit exposures have been obtained in stare mode.

The data for the TD LkCa15 have been obtained in the program Pr.Id. 288.C-5013 (PI Huelamo). We use in our analysis only 4 exposures obtained in one epoch (2011-12-01), which correspond to an entire ABBA slit-nodding cycle. Observations have been made using the 0.8x11" slit in the UVB arm, the 0.7x11" one in the VIS arm, and the 0.9x11" slit in the NIR arm. The readout mode used was "100,1x1,hg". Using only 4 frames we obtain a spectrum with enough S/N for our purpose.

2.3. Data reduction

Data reduction has been carried out using the version 1.3.7 of the X-Shooter pipeline (Modigliani et al., 2010), run through the *EsoRex* tool. The spectra were reduced independently for the three spectrograph arms. The pipeline takes into account, together with the standard reduction steps (i.e. bias or dark subtraction, flat fielding, spectrum extraction, wavelength calibration, and sky subtraction), also the flexure compensation and the instrumental profile. We checked with particular care the flux calibration and telluric removal of the spectra.

Telluric removal has been performed using the standard telluric spectra that have been provided as part of the standard X-Shooter calibration plan on each night of observations. Spectra of telluric standard stars observed at similar airmasses right before or after the target have been selected. The correction has been accomplished using the IRAF¹ task *telluric* adopting the same procedure for telluric normalization in the VIS and for response-function preparation in the NIR as explained by Alcalá et al. (2014).

Flux calibration has been carried out within the pipeline. Then, for the targets where only narrow-slit observations were available, we checked the flux-calibrated pipeline products comparing them with the available photometry to quantify slit losses. These spectra were then rescaled to the photometric data, and a final check was performed to verify a correct conjunctions between the three arms. The overall final agreement is very good. On the other hand, in the cases where observations with the large slit were available, we first checked that the flux-calibration of the spectra obtained with this slit were compatible with the available photometry. Then, we rescaled the narrow-slit spectra to the large-slit flux-calibrated ones, thus achieving the best possible flux calibration. Also in this case the final products have very good conjunctions between the arms.

¹ IRAF is distributed by National Optical Astronomy Observatories, which is operated by the Association of Universities for Research in Astronomy, Inc., under cooperative agreement with the National Science Foundation.

Table 1. Transitional disks observing log

Name	Other names	RA (2000) h m s	DEC (2000) ° ' "	OBS. DATE YY-MM-DD	T _{exp} (sec)			Pr.Id (PI)
					UVB	VIS	NIR	
LkHα330	...	03 45 48.29	32 24 11.9	2012-12-18	4x150	4x150	4x150	090.C-0050 (Manara)
DM Tau	...	04 33 48.74	18 10 09.7	2012-11-23	4x300	4x300	4x300	090.C-0050 (Manara)
LkCa15	...	04 39 17.79	22 21 03.4	2012-03-06	4x200	4x220	4x200	288.C-5013 (Huelamo)
GM Aur	...	04 55 10.98	30 21 59.3	2012-11-23	4x300	4x300	4x300	090.C-0050 (Manara)
SZ Cha	Ass Cha T 2-6	10 58 16.77	-77 17 17.0	2010-01-18	4x140	4x150	4x150	084.C-1095 (Herczeg)
TW Hya	...	11 01 51.91	-34 42 17.0	2010-05-03	4x150	4x60	4x100	085.C-0764 (Guenther)
CS Cha	ISO Cha I 3	11 02 24.91	-77 33 35.7	2010-01-18	2x55	2x60	2x60	084.C-1095 (Herczeg)
CHXR22E	...	11 07 13.30	-77 43 49.9	2010-01-19	2x280	2x300	2x300	084.C-1095 (Herczeg)
Sz18	Ass Cha T 2-25	11 07 19.15	-76 03 04.8	2010-01-17	2x60	2x53	2x60	084.C-1095 (Herczeg)
Sz27	Ass Cha T 2-35	11 08 39.05	-77 16 04.2	2010-01-18	2x410	2x420	2x420	084.C-1095 (Herczeg)
Sz45	Ass Cha T 2-56	11 17 37.00	-77 04 38.1	2010-01-17	2x45	2x40	2x45	084.C-1095 (Herczeg)
Sz84	...	15 58 02.53	-37 36 02.7	2012-04-18	2x350	2x300	2x115	089.C-0143 (Alcalà)
RX J1615-3255	2MASS J16152023-3255051	16 15 20.23	-32 55 05.1	2012-05-21	4x300	4x300	4x300	089.C-0840 (Manara)
Oph22	SSTc2d J162245.4-243124	16 22 45.40	-24 31 23.7	2012-04-25	4x600	4x600	4x600	089.C-0840 (Manara)
Oph24	SSTc2d J162506.9-235050	16 25 06.91	-23 50 50.3	2012-06-07	4x600	4x600	4x600	089.C-0840 (Manara)
SR 21	EM*SR21A, ISO-Oph 110	16 27 10.28	-24 19 12.7	2012-04-14	4x300	4x300	4x300	089.C-0840 (Manara)
ISO-Oph 196	WSB 60	16 28 16.51	-24 36 57.9	2010-07-28	4x750	4x750	4x750	085.C-0876 (Testi)
DoAr 44	...	16 31 33.46	-24 27 37.2	2010-05-03	4x300	4x140	4x150	085.C-0764 (Guenther)
Ser29	SSTc2d J182911.5+002039	18 29 11.50	00 20 38.6	2012-06-03	4x600	4x600	4x600	089.C-0840 (Manara)
Ser34	SSTc2d J182944.1+003356	18 29 44.11	00 33 56.0	2012-06-03	4x600	4x600	4x600	089.C-0840 (Manara)
RX J1842.9-3532	...	18 42 57.95	-35 32 42.7	2012-05-21	4x300	4x300	4x300	089.C-0840 (Manara)
RX J1852.3-3700	...	18 52 17.29	-37 00 11.9	2012-06-03	4x300	4x300	4x300	089.C-0840 (Manara)

Table 2. Class III YSOs properties and observing log

Name	Other names	RA (2000) h m s	DEC (2000) ° ' "	OBS. DATE YY-MM-DD	T _{exp} (sec)			SpT	T _{eff} [K]	A _V [mag]	d [pc]	L _* [L _⊙]	Pr.Id (PI)
					UVB	VIS	NIR						
IC348-127	Cl* IC 348 CPS 127	03 45 07.9	32 04 01.8	2012-11-11	4x150	4x150	4x150	G4	5800	6.0	320	12.9±5.9	090.C-0050 (Manara)
T21	Ass Cha T 2-21	11 06 15.4	-77 21 56.9	2010-01-19	2x70	2x60	2x60	G5	5770	3.2	160	18.5±8.5	084.C-1095 (Herczeg)
CrA75	RX J190222.0-365541	19 02 22.1	-36 55 40.9	2012-05-17	2x300	2x300	2x300	K2	4900	1.5	130	0.4±0.2	089.C-0840 (Manara)

3. Accretion and photospheric parameters

In the following, we briefly describe the procedure adopted to derive self-consistently from the complete X-Shooter spectrum SpT, A_V , and the accretion luminosity (L_{acc}) for our targets. The method is described in detail in Manara et al. (2013b) and is based on the fit of various parts of the observed spectra to derive these parameters. In particular, the analysis of the UV-excess together with that of absorption features at longer wavelengths allows us to determine properly the stellar properties and, at the same time, leads to an accurate and direct determination of the accretion properties. We then report the results obtained and compare these to the values derived in the literature.

3.1. Method description

Our method is based on a fitting procedure that considers the following three components to reproduce the observed spectrum. We include a range of photospheric template spectra - Class III YSOs from Manara et al. (2013a), augmented with some earlier SpT templates, as explained in Sect. 2.1.1 -. We consider a range of possible values for A_V , and we model the excess spectrum produced by the disk accretion process with a set of isothermal hydrogen slab emission spectra. The photospheric template spectrum and the slab model are normalized using two different normalization constants determined in the fitting procedure.

The best fit model is derived by minimizing a χ^2_{like} function defined as the sum of the squared deviations (data - model) divided by the error. The χ^2_{like} is computed in different regions of the UVB and VIS arms of the spectra, including the Balmer and Paschen continua region and some spectral regions around $\lambda \sim 700$ nm characterized by molecular features particularly strong in late-type stars. We also perform a visual check of the best fit in different photospheric features sensitive to the SpT of the target and veiled by the accretion emission.

The SpT of the best fit photospheric template is assumed for the input target with a typical uncertainty of one spectral subclass. The best fit determined A_V has an uncertainty $\lesssim 0.4$ mag, which takes into account both the uncertainty on the template A_V (0.3 mag; Manara et al., 2013a) and the one on the best-fit estimate (~ 0.2 mag; Manara et al., 2013b). We then derive L_{acc} by integrating the normalized best fit slab model spectrum from 50 nm to 2478 nm to include all the emission of the model. This value has an estimated uncertainty of ~ 0.2 dex (Manara et al., 2013b). The value of L_* is obtained from the luminosity of the best fit photospheric template after properly taking into account the normalization factor. The uncertainty on L_* , obtained considering the one on the L_* of the template (~ 0.2 dex; Manara et al., 2013a), on the best-fit, and on the distance, is ~ 0.25 dex.

From the SpT of the photospheric template we derive the T_{eff} of the object using the SpT- T_{eff} relation from Luhman et al. (2003) for M-type stars and Kenyon & Hartmann (1995) for earlier SpT objects. The stellar mass (M_*) is then derived by interpolating evolutionary models of Baraffe et al. (1998) in the position of the object on the HR Diagram, and its uncertainty is computed perturbing the position on the HR Diagram with the aforementioned uncertainty. Finally, \dot{M}_{acc} is derived using the classical relation $\dot{M}_{\text{acc}} = 1.25 \cdot L_{\text{acc}} R_*/(GM_*)$ (Hartmann et al., 1998), and this value has a typical uncertainty of ~ 0.4 dex, obtained propagating the uncertainties on R_* , M_* , and L_{acc} .

We adopt the reddening curve from Cardelli et al. (1989). The value of R_V , which is usually uncertain in young star forming regions, is assumed to be $R_V=5.5$ for CrA (Peterson et al., 2011, and reference therein) and $R_V=3.1$ for the other regions.

In particular, the analysis of the best fit results for the objects located in the ρ -Ophiucus region show that the use of the standard extinction curve at optical wavelength is more appropriate to reproduce the observations of our targets. Also for objects located in the Chameleon I region we find that the standard value $R_V=3.1$ better describes the observed spectrum of T21, as we reported in Sect. 2.1.1.

In addition to the fitting of the UVB and VIS arms of our spectra described above, we also perform a check of the best fit results using the NIR arm spectra, i.e. at $\lambda \gtrsim 1000$ nm. For definition, TDs have low or negligible emission in excess to the photosphere at near-infrared wavelengths, and strong excess at mid-infrared and far-infrared wavelengths (e.g., Calvet et al., 2005). For this reason, we expect our best fit photospheric template to match the target spectrum also in the NIR arm. This does not apply when fitting PTDs, where the contribution of inner-disk emission at near-infrared wavelengths, which is not included in our models, is not negligible. In the latter case we expect the photospheric template spectrum to lay below the target one in the near-infrared. In this check we include also, when available, the $3.6 \mu\text{m}$ Spitzer magnitude of the object, after correcting it for extinction following the prescription of McClure (2009), and the magnitude of the template. The analysis of the IR color excess will be described in detail in Sect. 3.2. The best fit stellar and accretion parameters for the targets are reported in Table 3.

Finally, we use the relations between the luminosity of some emission lines (L_{line}) and L_{acc} calibrated by Alcalá et al. (2014) to verify our derived parameters. If the best fit L_{acc} and A_V are correct, we expect to derive compatible values of L_{acc} from the luminosity of emission lines located in different parts of the spectra with no particular wavelength dependence. We select for this check the following 5 emission lines spread along the whole spectrum: $H\alpha$ (λ 656.3 nm), $H\beta$ (λ 486.1 nm), $H\gamma$ (λ 434.0 nm), $\text{Pa}\beta$ (λ 1281.8 nm), and $\text{Br}\gamma$ (λ 2166.1 nm). We report the fluxes of these lines in Table 4. We collect in the same table also the equivalent width (EW) of the lithium line at λ 670.8 nm, that is an indicator of young ages and confirms the YSO status of all our objects.

In Manara et al. (2013b), Alcalá et al. (2014), and Rigliaco et al. (2012) the procedure described above has been tested on low-mass stars with SpT later than $\sim K5$. We show here its validity also for YSOs with early-K SpT. As reported in Sect. 2.1.1, we stress that the sample of Class III YSOs available is highly incomplete when considering objects with SpT in the interval from G5 to K5, given that we have at disposal only one Class III YSO with SpT K2. Finally, a more detailed analysis is needed for objects with G-type SpT, the so-called intermediate mass stars, because for these objects the excess emission due to accretion can be hardly detected in the wavelength region covered by X-Shooter (e.g. Calvet et al., 2004). We thus discuss in the following sections these three different types of objects separately.

3.1.1. Results for low mass stars

The best fits obtained for TDs with M SpT are shown in Fig. 1, while those for TDs with SpT later or equal to K5 in Fig. 2. The observed and reddening corrected spectra are shown with a red line, the green line represents the photospheric templates used, the light blue line the slab model, and the blue line the best fit, which is the sum of the photospheric template and the slab model. The best fit is plotted only in the regions where it is calculated, i.e. $\lambda \sim 330$ -1000 nm. The agreement between the best fit and the observed spectrum in this wavelength range is always very good. At wavelengths longer than ~ 1000 nm we plot only

the photospheric template and the observed spectra, including also their $3.6\ \mu\text{m}$ Spitzer magnitudes, when available. As mentioned earlier, we expect the photospheric template spectrum not to exceed the target one in this region. This is the case for most of the targets, but not for Oph22, Oph24, DM Tau, and GM Aur. For one object, Sz27, the excess emission at near-infrared wavelengths confirms the previous classification as PTD. According to our best fits, also CHXR22E and ISO-Oph 196 should be classified as PTD.

The stellar and accretion parameters obtained for these targets are reported in Table 3. For the objects considered in this section, i.e. with SpT later or equal to K5, the best fit SpT is the same within up to one or two spectral sub-class as the one reported in the literature. In most cases the difference with respect to the literature values is small also for the other stellar and accretion parameters. In particular, values of \dot{M}_{acc} agree within 0.3 dex with those reported in the literature. The objects with larger differences are Sz18, Sz45, RX J1615, Oph24, Ser29, and Ser34. We suggest that these differences are due to the different methodologies of previous studies with respect to our. Variability of accretion would result in a smaller difference. Recent studies showed that in most young accreting stars these variations are in general smaller than 0.3 dex (e.g., Costigan et al., 2012). For Ser29 we are only able to provide an upper limit on L_{acc} from the fitting due to the low signal-to-noise of the spectrum in the whole UVB arm. This value is compatible with the measurement of the $H\alpha$ line, which is the only line seen in emission in the spectrum.

3.1.2. Results for early K-type stars

For six of our objects we obtain a best fit using the Class III YSO template with SpT K2. These results are also reported in Table 3, while their best fit are shown in Fig. 3. In all these cases the best fit is very good with the only exception of RX J1852.3. With respect to the literature, typical differences of the SpT from the best fit K2 are of up to two spectral sub-classes apart from CS Cha, which was previously classified as K6. We adopt for all these targets SpT K2 in our analysis, with the caveat that the uncertainty on this parameter is larger for these objects with respect to later SpT targets due to the already mentioned incompleteness of photospheric templates of SpT late-G and early-K. Our best fits confirm that DoAr44, LkCa15, and SzCha are PTD (see also Sect. 3.2). We find a hint of excess in the K-band spectrum of RX J1842.9, which becomes clearer at the Spitzer [3.6] data point. This confirms the observations of infrared excess in this object reported in Hughes et al. (2010) and implies that also this object is a PTD. The largest difference in the derived values of \dot{M}_{acc} is for SzCha, which results to be a stronger accretor than previously determined.

3.1.3. Results for intermediate-mass stars

Two objects in our sample are of early-G SpT, namely LkH α 330 and SR21. For these TDs we have not been able to detect excess emission with our fitter. As also Calvet et al. (2004) pointed out, the excess emission for intermediate-mass stars like these two is hard to be detected at $\lambda > 330\ \text{nm}$ due to the similar temperatures of the accretion shock and the stellar photosphere. We have only been able to fit these spectra to derive their A_V and L_* , and we show these best fits in Fig. 4. Their positions on the HRD are not covered by the evolutionary tracks of Baraffe et al. (1998), so we derive the values of M_* for these two targets using the models of D’Antona & Mazzitelli (1994). In both objects we detect an

excess emission in the near-infrared wavelengths which could imply these objects are PTD.

In the spectrum of LkH α 330 various emission lines are present, such as the $H\alpha$, $H\beta$, $\text{Pa}\beta$, and $\text{Br}\gamma$. The only $L_{\text{acc}}-L_{\text{line}}$ relation available for this class of objects is the one reported in Calvet et al. (2004) for the $\text{Br}\gamma$ line. We use this relation to derive a value of $L_{\text{acc}} \sim 0.23\ L_{\odot}$ which leads to a value of \dot{M}_{acc} consistent with those reported in the literature.

The hydrogen recombination lines of SR21 appear in absorption in the whole spectrum. The same is found when looking at the CaII IRT lines. Moreover, the photospheric lines of this object appear much broader than the corresponding Class III YSO spectrum. Nevertheless, the wings of the hydrogen lines, in particular those of the $H\alpha$ line, appear in emission at very high velocities up to $\sim 250\ \text{km/s}$, thus suggesting that they originate in an accretion-related infall region. Therefore we classify this object as an accreting TD. Given that no $\text{Br}\gamma$ emission is detected in this spectrum, we derive L_{acc} from the luminosity of the $H\alpha$ line. This is derived from the dereddened spectrum corrected for the photospheric line contribution, which is estimated using a synthetic spectrum of the same T_{eff} and broaden to match photospheric lines close to the $H\alpha$. To convert the luminosity of the $H\alpha$ line in L_{acc} we use the relation provided by Alcalá et al. (2014). Given all the assumptions adopted to estimate this value we consider the derived L_{acc} very uncertain.

3.2. Infrared color excess

From the best fit derived as explained above we analyze the color excess in the IR colors in order to detect emission from the innermost dusty disk. We perform synthetic photometry on the dereddened TD spectra and on the Class III YSO spectra. We then plot in Fig. 5-6 the $J - K$ and $J - [3.6]$ colors as a function of T_{eff} both for the Class III YSOs (*red circles*) and the TDs (*blue crosses*). These colors trace the presence of an inner disk, which would result in an excess emission with respect to the photosphere in the K band and at $3.6\ \mu\text{m}$. As a reference, we plot with a dashed line the photospheric color locus of diskless YSOs derived by Luhman et al. (2010). We see that the colors of the Class III YSOs are distributed on these plots around this empirically calibrated locus with a small dispersion. Also most of the TDs have colors compatible with the Class III YSOs at the same T_{eff} , meaning that their IR colors are compatible with photospheric ones, thus they have no dust-rich inner disk. In some cases, however, the excess is detectable and the objects should be classified as PTD. This is the case for the objects already listed in the previous sections, namely ISO Oph 196, CHXR22E, Sz 27, DoAr 44, Sz Cha, LkCa15, RX J1842.9, LkH α 330, and SR21, and for GM Aur, given the excess in the $J - [3.6]$ color (see Fig. 6). This object was also previously classified as PTD by Calvet et al. (2005) and Espaillat et al. (2010). For one object, CS Cha, the excess is detected in the $J - K$ color but not in the $J - [3.6]$ one, and in the former it is compatible with the Class III YSOs color. We thus classify this object as TD. We report this classification in Table 3. The objects classified as PTD have R_{in} values that range smoothly from 5 to 68 AU. The presence of a dusty innermost region of the disk is thus uncorrelated with the size of the dust-depleted gap.

4. Wind signatures

The most prominent forbidden line present in the spectra of our TDs is the [OI] $\lambda\ 630\ \text{nm}$ line. This line has been detected in many accreting YSOs (e.g., Hartigan et al., 1995) and can

M-type transitional disks

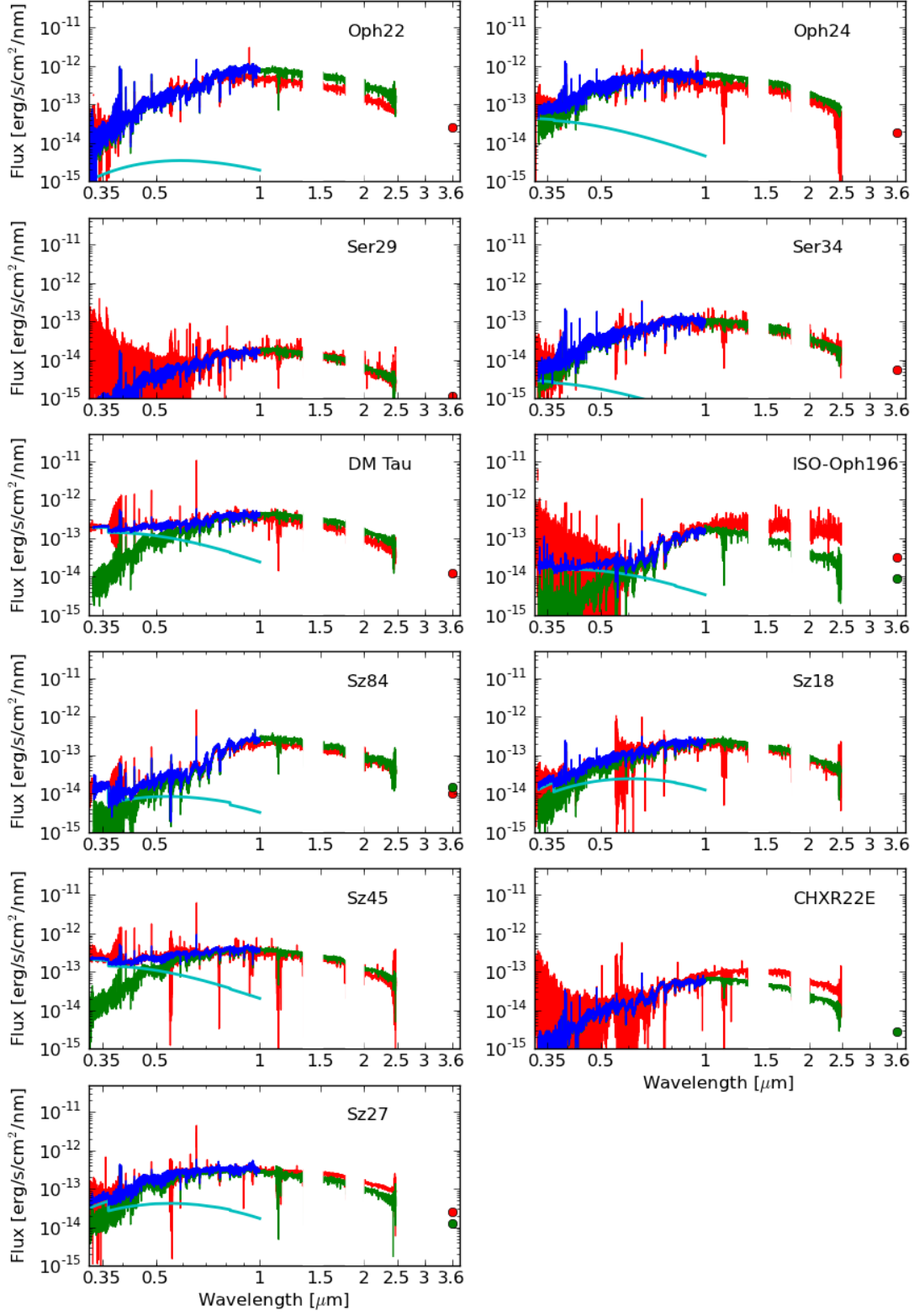


Fig. 1. Best fit for transitional disks with spectral type in the M class. The red line is the observed dereddened spectrum, green line the photospheric template, light blue line the slab model, and blue line the best fit.

late K-type transitional disks

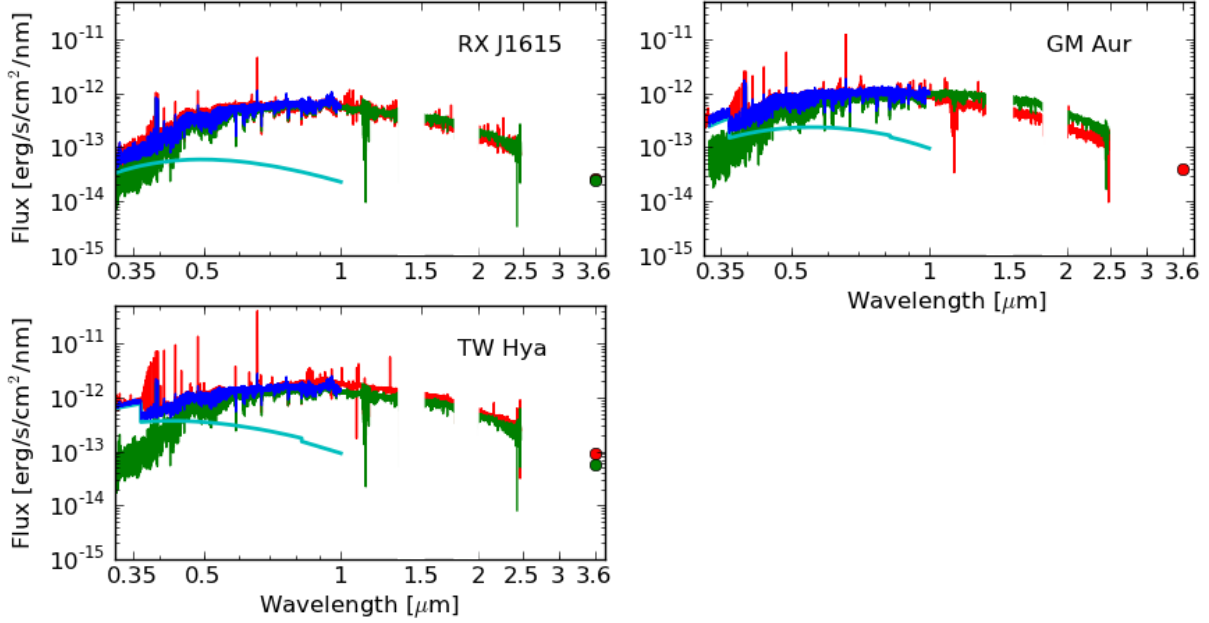


Fig. 2. Best fit for late-K type transitional disks. Colors as in Fig. 1

Table 3. Stellar, disk, and accretion parameters of the targets

Name	dist [pc]	R_{in} [AU]	SpT	T_{eff} [K]	A_V [mag]	L_* [L_\odot]	$\log L_{acc}$ [L_\odot]	M_* [M_\odot]	$\log \dot{M}_{acc}$ [M_\odot/yr]	R_* [R_\odot]	Disk type	Ref
LkH α 330	250	68	G4	5800	3.0	14.40	-0.6	2.35 ± 0.57	-7.8	3.74 ± 1.08	PTD	1 D
DM Tau	140	19	M2	3560	1.1	0.36	-1.3	0.56 ± 0.08	-8.2	1.57 ± 0.46	TD	1 B
LkCa 15	140	50	K2	4900	1.2	1.21	-1.1	1.24 ± 0.33	-8.4	1.52 ± 0.44	PTD	1 B
GM Aur	140	28	K5	4350	0.6	0.99	-1.0	1.36 ± 0.36	-8.3	1.75 ± 0.51	PTD	1 B
Sz-Cha	160	29	K2	4900	1.3	1.17	-0.5	1.22 ± 0.32	-7.8	1.50 ± 0.43	PTD	2 B
TW Hya	55	4	K7	4060	0.0	0.18	-1.6	0.79 ± 0.17	-8.9	0.85 ± 0.25	TD	3 B
CS Cha	160	43	K2	4900	0.8	1.45	-1.0	1.32 ± 0.37	-8.3	1.66 ± 0.48	TD	4 B
CHXR22E	160	7	M4	3270	2.6	0.07	-4.1	0.24 ± 0.06	-10.9	0.82 ± 0.24	PTD	2 B
Sz18	160	8	M2	3560	1.3	0.26	-1.9	0.54 ± 0.08	-8.9	1.34 ± 0.39	TD	2 B
Sz27	160	15	K7	4060	2.9	0.33	-1.6	0.96 ± 0.24	-8.9	1.16 ± 0.34	PTD	2 B
Sz45	160	18	M0.5	3780	0.7	0.42	-1.2	0.85 ± 0.11	-8.3	1.51 ± 0.44	TD	2 B
Sz84	150	55	M5	3125	0.5	0.24	-2.3	0.24 ± 0.06	-8.9	1.67 ± 0.49	TD	5 B
RX J1615	185	30	K7	4060	0.0	0.89	-1.3	1.16 ± 0.16	-8.5	1.90 ± 0.55	TD	1 B
Oph22	125	1	M3	3415	3.0	0.56	-2.9	0.53 ± 0.14	-9.7	2.13 ± 0.62	TD	5 B
Oph24	125	3	M0	3850	4.0	0.42	-2.0	0.92 ± 0.13	-9.2	1.45 ± 0.42	TD	5 B
SR 21	125	36	G4	5800	6.0	8.11	-0.7 ^a	1.95 ± 0.50	-7.9 ^a	2.81 ± 0.81	PTD	1 D
ISO-Oph196	125	15	M5.5	3060	3.0	0.08	-2.3	0.14 ± 0.04	-8.9	1.00 ± 0.29	PTD	1 B
DoAr 44	125	30	K2	4900	1.7	0.64	-0.9	0.97 ± 0.19	-8.2	1.11 ± 0.32	PTD	1 B
Ser29	230	8	M2	3560	2.6	0.04	<-3.8	0.47 ± 0.08	<-11.2	0.52 ± 0.15	TD	5 B
Ser34	230	25	M1	3705	2.7	0.26	-2.7	0.71 ± 0.08	-9.8	1.23 ± 0.36	TD	5 B
RX J1842.9	130	5	K2	4900	0.4	0.56	-1.5	0.93 ± 0.16	-8.8	1.03 ± 0.30	PTD	6 B
RX J1852.3	130	16	K2	4900	1.0	0.77	-1.4	1.04 ± 0.19	-8.7	1.21 ± 0.35	TD	6 B

Notes. Reference for R_{in} : (1) Andrews et al. (2011), (2) Kim et al. (2009), (3) Hughes et al. (2007), (4) Espaillat et al. (2013), (5) Merín et al. (2010), (6) Hughes et al. (2010). Evolutionary models used to derive M_* and \dot{M}_{acc} : (B) Baraffe et al. (1998), (D) D’Antona & Mazzitelli (1994). ^aHighly uncertain value.

present two distinct components. The high-velocity component (HVC, $\Delta v \sim 100\text{--}200 \text{ km s}^{-1}$) of this line is known to trace collimated jets. The origin of the low-velocity component (LVC, $\Delta v \sim 2\text{--}3 \text{ km s}^{-1}$), instead, is still unclear. It is believed to originate in the disk or from the base of a slow disk wind (Hartigan et al., 1995), but there are suggestions that it can be originated in a photoevaporative wind (Rigliaco et al., 2013, and references therein). We detect the LVC of this line in 17 ($\sim 80\%$) of the

spectra of our TDs, with a clear detection of the HVC only in ISO-Oph 196.

We derive the flux and the peak velocity of the LVC of the [OI] λ 630 nm line in the following way. We firstly refine the wavelength calibration by fitting the photospheric Li I line at λ 670.78 nm and shifting the spectra to match the nominal central wavelength of this line. This line is detected in all the objects and its EW are reported in Column 7 of Table 4. Then, we fit

early K-type transitional disks

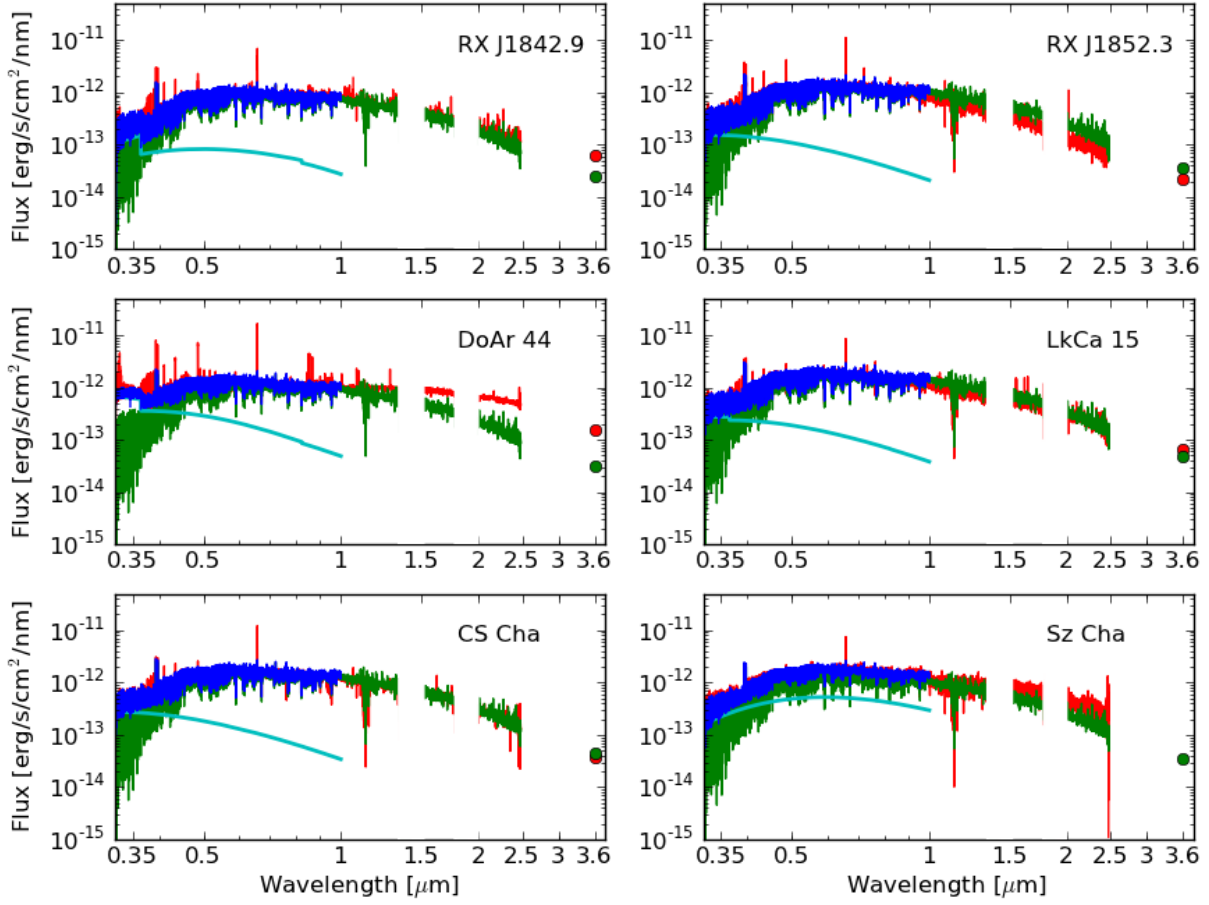


Fig. 3. Best fit of early K-type transitional disks. Colors as in Fig. 1

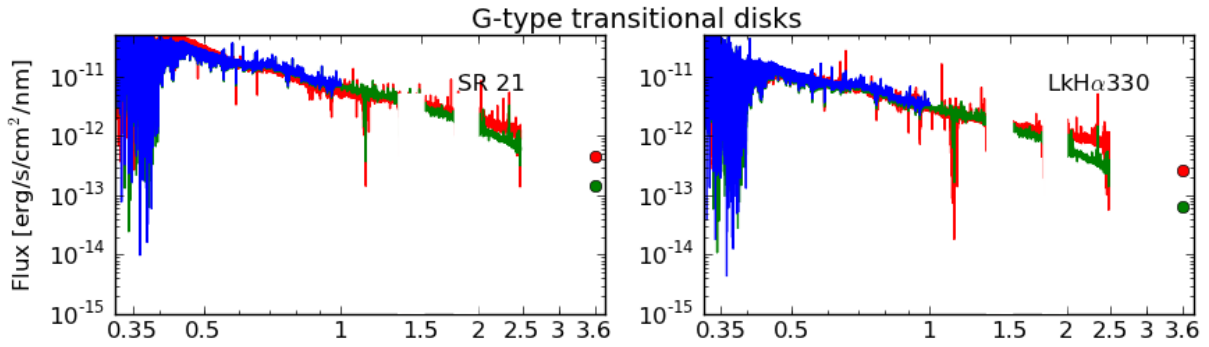


Fig. 4. Best fit of G-type transitional disks. Colors as in Fig. 1.

with a gaussian profile on the dereddened spectrum the LVC of the $[OI]\lambda 630$ nm line and we integrate the flux of the best fit to derive the line flux. The error on the flux is derived from the standard deviation of the continuum estimated around the line. The derived flux, error, peak velocity (v_0), and FWHM of the gaussian fit is reported in Table 5. The lines and their best fits are shown in Fig. 7. In all the objects with detected $[OI]\lambda 630$ nm line, with the exception of LkH α 330, the line is slightly blueshifted, with values of v_0 ranging from ~ -2 km/s to ~ -8 km/s in most cases, and only two objects (Oph24 and ISO-Oph

196) with $v_0 < -10$ km/s. Even if the exact value of v_0 in each object is still uncertain also after the procedure to correct the wavelength calibration described above, we see that the $[OI]\lambda 630$ nm line is systematically blueshifted, meaning that it is originated in some kind of wind. The mean value of the FWHM of the $[OI]\lambda 630$ nm line derived from the spectra of our targets is ~ 40 km/s. We note, however, that the values of FWHM $\lesssim 30$ km/s should be considered with caution, as these values are close to the nominal resolution of the instrument.

Table 4. Derived properties of analyzed lines

Name	$F_{H\alpha}$ [$\text{erg s}^{-1} \text{cm}^{-2}$]	$F_{H\beta}$ [$\text{erg s}^{-1} \text{cm}^{-2}$]	$F_{H\gamma}$ [$\text{erg s}^{-1} \text{cm}^{-2}$]	$F_{Pa\beta}$ [$\text{erg s}^{-1} \text{cm}^{-2}$]	$F_{Br\gamma}$ [$\text{erg s}^{-1} \text{cm}^{-2}$]	$EW_{Li_{670.8}}$ [mÅ]
LkHa330	$(1.11 \pm 0.02) \times 10^{-11}$	$(6.6 \pm 2.9) \times 10^{-13}$	$< 3.2 \times 10^{-13}$	$(6.5 \pm 0.3) \times 10^{-13}$	$(5.9 \pm 3.4) \times 10^{-14}$	110 ± 2
DM Tau	$(4.48 \pm 0.02) \times 10^{-12}$	$(3.5 \pm 0.1) \times 10^{-13}$	$(2.2 \pm 0.1) \times 10^{-13}$	$(1.06 \pm 0.07) \times 10^{-13}$	$(1.4 \pm 0.2) \times 10^{-14}$	410 ± 21
LkCa 15	$(3.1 \pm 0.1) \times 10^{-12}$	$(3.7 \pm 1.6) \times 10^{-13}$	$(1.5 \pm 0.1) \times 10^{-13}$	$(1.2 \pm 0.2) \times 10^{-13}$	$(1.9 \pm 1.5) \times 10^{-14}$	460 ± 23
GM Aur	$(1.06 \pm 0.02) \times 10^{-11}$	$(2.1 \pm 0.07) \times 10^{-12}$	$(7.9 \pm 0.4) \times 10^{-13}$	$(1.01 \pm 0.02) \times 10^{-12}$	$(1.6 \pm 0.1) \times 10^{-13}$	440 ± 22
Sz Cha	$(2.6 \pm 0.1) \times 10^{-12}$	$< 4.7 \times 10^{-14}$	$< 4.0 \times 10^{-14}$	$(1.9 \pm 0.3) \times 10^{-13}$	$< 1.3 \times 10^{-14}$	350 ± 10
TW Hya	$(2.39 \pm 0.04) \times 10^{-11}$	$(4.52 \pm 0.07) \times 10^{-12}$	$(2.2 \pm 0.05) \times 10^{-12}$	$(2.21 \pm 0.04) \times 10^{-12}$	$(2.61 \pm 0.08) \times 10^{-13}$	430 ± 21
CS Cha	$(5.23 \pm 0.09) \times 10^{-12}$	$(4.7 \pm 1.1) \times 10^{-13}$	$(2.2 \pm 0.4) \times 10^{-13}$	$(1.1 \pm 0.1) \times 10^{-13}$	$(2.6 \pm 1.1) \times 10^{-14}$	510 ± 28
CHXR22E	$(1.1 \pm 0.1) \times 10^{-14}$	$(4.4 \pm 0.6) \times 10^{-15}$	$(9.1 \pm 4.9) \times 10^{-16}$	$< 9.1 \times 10^{-15}$	$< 2.4 \times 10^{-15}$	230 ± 56
Sz18	$(3.8 \pm 0.2) \times 10^{-13}$	$(2.5 \pm 0.6) \times 10^{-14}$	$(7.9 \pm 0.9) \times 10^{-15}$	$(4.3 \pm 1.7) \times 10^{-15}$	$< 2.7 \times 10^{-15}$	590 ± 77
Sz27	$(1.83 \pm 0.08) \times 10^{-12}$	$(7.8 \pm 0.6) \times 10^{-14}$	$(3.2 \pm 0.2) \times 10^{-14}$	$(4.9 \pm 0.5) \times 10^{-14}$	$(1.0 \pm 0.2) \times 10^{-14}$	510 ± 29
Sz45	$(2.83 \pm 0.02) \times 10^{-12}$	$(4.6 \pm 0.1) \times 10^{-13}$	$(2.9 \pm 0.1) \times 10^{-13}$	$(1.17 \pm 0.08) \times 10^{-13}$	$(2.0 \pm 0.5) \times 10^{-14}$	440 ± 32
Sz84	$(7.0 \pm 0.1) \times 10^{-13}$	$(5.59 \pm 0.09) \times 10^{-14}$	$(2.7 \pm 0.04) \times 10^{-14}$	$(3.1 \pm 0.3) \times 10^{-14}$	$(1.1 \pm 0.5) \times 10^{-14}$	460 ± 20
RX J1615	$(2.24 \pm 0.05) \times 10^{-12}$	$(2.5 \pm 0.3) \times 10^{-13}$	$(6.9 \pm 1.1) \times 10^{-14}$	$(7.5 \pm 1.6) \times 10^{-14}$	$(1.5 \pm 0.7) \times 10^{-14}$	550 ± 32
Oph22	$(1.9 \pm 0.09) \times 10^{-13}$	$(5.4 \pm 0.1) \times 10^{-14}$	$(2.8 \pm 0.1) \times 10^{-14}$	$< 1.7 \times 10^{-14}$	$< 7.3 \times 10^{-15}$	570 ± 40
Oph24	$(3.2 \pm 0.2) \times 10^{-13}$	$(1.08 \pm 0.03) \times 10^{-13}$	$(7.7 \pm 0.3) \times 10^{-14}$	$< 6.4 \times 10^{-14}$	$(5.0 \pm 1.5) \times 10^{-15}$	570 ± 37
SR 21 ^a	140 ± 2
ISO–Oph196	$(3.54 \pm 0.01) \times 10^{-13}$	$(8.8 \pm 0.6) \times 10^{-14}$	$(8.8 \pm 0.8) \times 10^{-14}$	$< 7.4 \times 10^{-14}$	$(2.2 \pm 0.3) \times 10^{-14}$	370 ± 31
DoAr 44	$(9.4 \pm 0.1) \times 10^{-12}$	$(2.66 \pm 0.08) \times 10^{-12}$	$(1.04 \pm 0.06) \times 10^{-12}$	$(1.12 \pm 0.01) \times 10^{-12}$	$(2.6 \pm 0.1) \times 10^{-13}$	420 ± 19
Ser29	$(1.3 \pm 0.1) \times 10^{-14}$	$< 1.7 \times 10^{-15}$	$< 8.0 \times 10^{-15}$	$< 1.9 \times 10^{-15}$	$< 4.8 \times 10^{-17}$	380 ± 199
Ser34	$(1.02 \pm 0.05) \times 10^{-13}$	$(7.8 \pm 0.7) \times 10^{-15}$	$(5.9 \pm 1.1) \times 10^{-15}$	$< 1.6 \times 10^{-15}$	$(1.8 \pm 0.4) \times 10^{-15}$	630 ± 40
RX J1842.9	$(3.41 \pm 0.08) \times 10^{-12}$	$(4.6 \pm 0.6) \times 10^{-13}$	$(2.0 \pm 0.2) \times 10^{-13}$	$(1.2 \pm 0.1) \times 10^{-13}$	$(1.5 \pm 0.7) \times 10^{-14}$	440 ± 21
RX J1852.3	$(5.67 \pm 0.09) \times 10^{-12}$	$(1.01 \pm 0.07) \times 10^{-12}$	$(2.8 \pm 0.4) \times 10^{-13}$	$(2.0 \pm 0.2) \times 10^{-13}$	$(4.0 \pm 2.5) \times 10^{-14}$	510 ± 30

Notes. Fluxes are reported in the format (flux \pm err) multiplied by the order of magnitude. ^aThe estimate of the flux of the emission lines of SR21 is very uncertain, thus we do not report these values for this object.

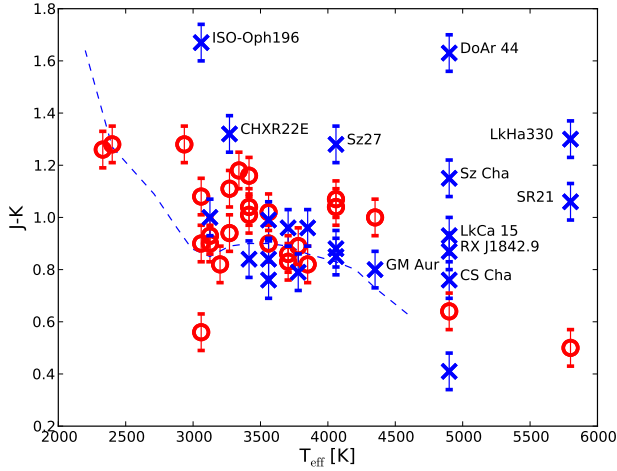


Fig. 5. $J - K$ color calculated with synthetic photometry on the best fit dereddened TD spectra (*blue crosses*) vs T_{eff} of the targets. The *red circles* represent the Class III YSOs colors derived with synthetic photometry on their spectra. The dashed line represents the photospheric color of YSOs according to Luhman et al. (2010).

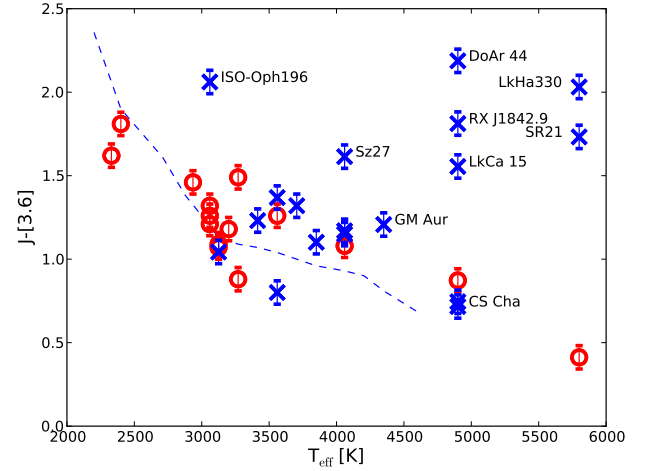


Fig. 6. $J - [3.6]$ color vs T_{eff} of the targets. The J magnitude is calculated on the best-fit dereddened TD spectra (*blue crosses*), while the $[3.6]$ magnitude is derived from the literature. Colors and symbols are the same as in Fig. 5.

5. Discussion

In this section we discuss the accretion and wind properties of our targets and we estimate the amount of gaseous material in their inner disks. It should be kept in mind that our sample is composed mostly by objects already known to be strong accretors and it is *not* an unbiased sample. Nevertheless, the properties of these strong-accreting TDs have important consequences

on our understanding of the TDs formation and evolution, as we discuss in the following.

5.1. Accretion properties

Here we aim at understanding whether there is a dependence of the accretion properties of our objects with the morphology of the disk, in particular with R_{in} , and whether there are differences with respect to accretion properties in cTTs.

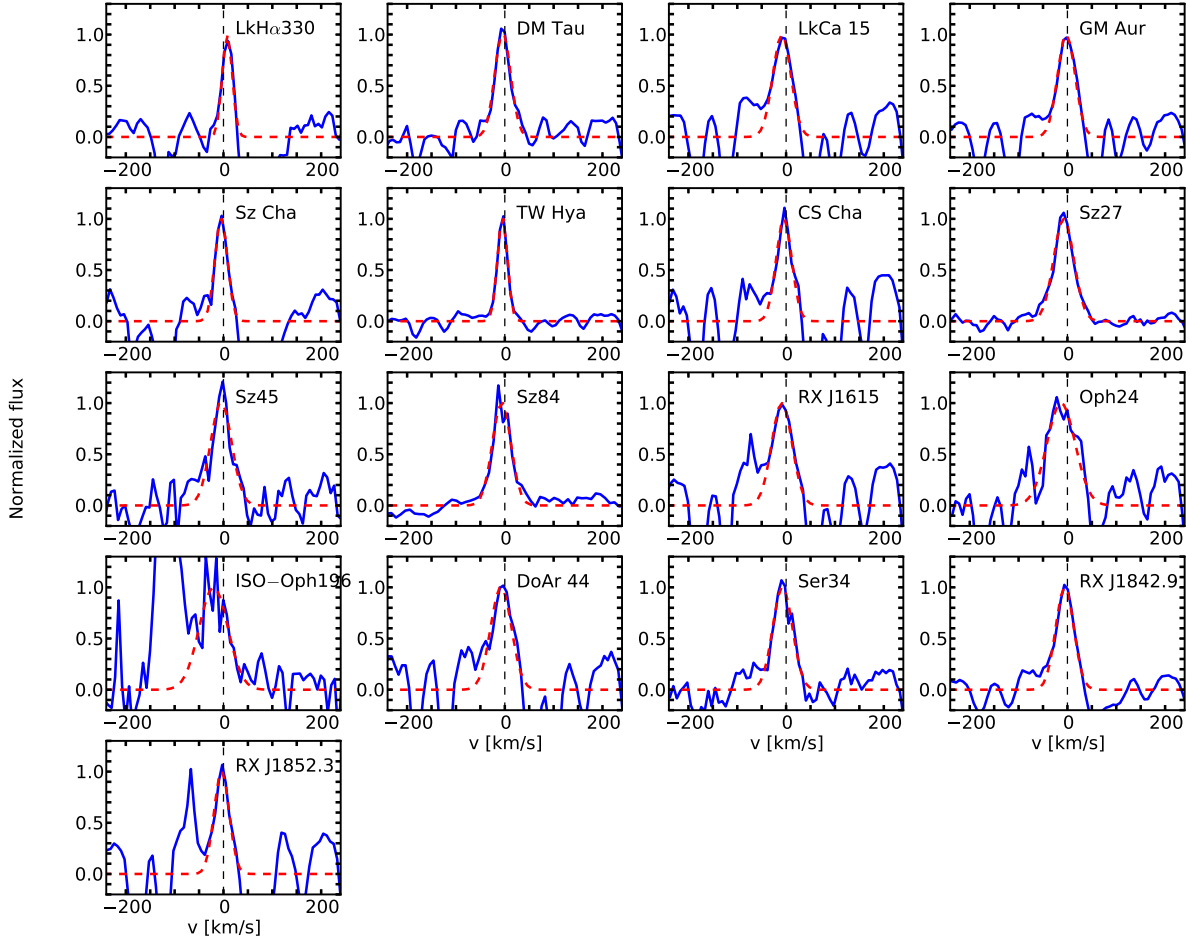


Fig. 7. Normalized [OI] 630 nm line for the TDs in our sample where this line has been detected. The red dashed line is the best gaussian fit of the low-velocity component of the line.

In Fig. 8 we show the logarithmic values of \dot{M}_{acc} determined in Sect. 3 as a function of the values of R_{in} reported in the literature (see Table 3). We represent these values using different symbols to differentiate measurement of R_{in} derived with resolved mm-interferometry observations (*red circles*) from those obtained by modeling the optical to mid-infrared SEDs (*blue squares*). The uncertainties on the values of R_{in} are various and depend strongly on the assumptions on the models. In particular, values of R_{in} determined with SED fitting are strongly model-dependent and can be an overestimation of the real gap size (Rodgers-Lee et al., 2014). We do not find any strong trend of \dot{M}_{acc} increasing with R_{in} over the whole range of R_{in} we have explored. If we compare our results with more complete samples of TDs, e.g., Kim et al. (2013), we see that our results agree with the upper boundary of their sample, and that indeed there is an increase of \dot{M}_{acc} with R_{in} up to values of $R_{\text{in}} \sim 20$ AU. At R_{in} larger than about 20 AU, however, \dot{M}_{acc} is essentially constant in our sample. In fact, a similar trend is also present in the upper envelope of the TDs considered in Kim et al. (2013), where, however, there are just two accreting TDs with $\dot{M}_{\text{acc}} > 10^{-8} M_{\odot}/\text{yr}$ for $R_{\text{in}} \gtrsim 20$ AU and none for $R_{\text{in}} \gtrsim 30$ -40 AU. All objects in our sample

have \dot{M}_{acc} in the range $10^{-9} - 10^{-8} M_{\odot}/\text{yr}$, independently of the value of R_{in} . Therefore, the density of their innermost gaseous disk, which accretes onto the star, does not depend on the mechanism that produces the gap or the hole, and must be high enough to sustain the observed accretion rates.

We want now to compare the derived values of \dot{M}_{acc} for our sample of TDs with a sample of classical T Tauri stars (cTTs) to determine whether the accretion properties are different in these two classes of objects. It is well established that the values of \dot{M}_{acc} in cTTs depend on M_{\star} with a power of ~ 1.6 -1.8 (e.g., Muzerolle et al., 2003; Rigliaco et al., 2011; Manara et al., 2012; Alcalá et al., 2014; Ercolano et al., 2014). A comparison of the values of \dot{M}_{acc} between different samples should be based on a comparison of this relation and not on the values of \dot{M}_{acc} alone. Another well known dependence is the one between \dot{M}_{acc} and the age of the targets (e.g., Hartmann et al., 1998; Sicilia-Aguilar et al., 2010; Manara et al., 2012), which is a consequence of the viscous evolution of protoplanetary disks. Therefore, a comparison should be carried out between objects of similar mean age. Finally, different methodology and evolutionary models can lead to different values of \dot{M}_{acc} ; it is thus needed to compare samples

Table 5. Derived properties of [OI] line at λ 630 nm

Name	$F_{[\text{OI}]\lambda 630}$ [erg s ⁻¹ cm ⁻²]	$v_{0,[\text{OI}]\lambda 630}$ [km/s]	$\text{FWHM}_{[\text{OI}]\lambda 630}$ [km/s]
LkH α 330	$(6.1 \pm 1.9) \times 10^{-14}$	7.7	24
DM Tau	$(9.1 \pm 1.8) \times 10^{-15}$	-4.3	38
LkCa 15	$(4.6 \pm 1.9) \times 10^{-14}$	-8.7	43
GM Aur	$(3.9 \pm 1.0) \times 10^{-14}$	-2.2	42
Sz Cha	$(2.4 \pm 0.9) \times 10^{-14}$	-4.7	30
TW Hya	$(9.0 \pm 0.8) \times 10^{-14}$	-4.8	24
CS Cha	$(2.8 \pm 1.5) \times 10^{-14}$	-4.4	37
CHXR22E	$< 8.0 \times 10^{-16}$
Sz18	$< 2.6 \times 10^{-15}$
Sz27	$(5.4 \pm 0.3) \times 10^{-14}$	-7.6	49
Sz45	$(1.8 \pm 0.5) \times 10^{-14}$	-4.8	50
Sz84	$(2.4 \pm 0.2) \times 10^{-15}$	-6.5	44
RX J1615	$(1.7 \pm 0.8) \times 10^{-14}$	-8.7	49
Oph22	$< 7.3 \times 10^{-15}$
Oph24	$(3.0 \pm 1.3) \times 10^{-14}$	-13.0	67
SR 21	$< 6.4 \times 10^{-14}$
ISO-Oph196	$(1.4 \pm 0.4) \times 10^{-15}$	-20.4	68
DoAr 44	$(2.6 \pm 1.2) \times 10^{-14}$	-7.7	50
Ser29	$< 4.2 \times 10^{-16}$
Ser34	$(4.1 \pm 0.8) \times 10^{-15}$	-7.3	47
RX J1842.9	$(5.0 \pm 0.8) \times 10^{-14}$	-5.5	43
RX J1852.3	$(2.6 \pm 1.3) \times 10^{-14}$	-3.8	36

Notes. Fluxes are reported in the format (flux \pm err) multiplied by the order of magnitude.

analyzed with a similar methodology. For these reasons we select as a comparison sample the objects studied by Alcalá et al. (2014). These are located in the Lupus I and III clouds and have ages ~ 3 Myr, similar to the objects in our sample. The analysis of that sample was carried out with the same methodology as the one we used here. We show in Fig. 9 the logarithmic relation between \dot{M}_{acc} and M_* for these two samples. Our data are reported as blue circles, while data from Alcalá et al. (2014) as green diamonds. The solid line on the plot is the best fit relation from Alcalá et al. (2014), and the dashed lines represent the dispersion of 0.4 dex around this best fit relation. The typical errors on the quantities are shown as a black cross. We see that $\sim 80\%$ of the TDs have values of \dot{M}_{acc} consistent with the values found by Alcalá et al. (2014) for Lupus objects of the same M_* . Therefore, for these objects we do not see any difference in the accretion properties with respect to those in cTTs. We also perform on these two samples a Kolmogorov-Smirnov statistical test (K-S test). When restricting to objects in the same M_* range the probability that the two samples are drawn from the same distribution is 80%. We can then conclude that for our sample, the amount of accretion depends on the mass of the central object, and not on the evolutionary stage (cTTs or TD) of the system.

This result differs from what found in the literature. For example, Najita et al. (2007) noted that TDs have a systematically smaller value of \dot{M}_{acc} at any given value of the mass of the disk (M_d). They inferred that the accretion rates for TDs are in general smaller than for cTTs. Similarly, various further analyses of larger samples of TDs found values of \dot{M}_{acc} typically lower than those of cTTs by a factor ~ 10 (e.g., Kim et al., 2009, 2013; Muzerolle et al., 2010; Espaillat et al., 2012). These results are reported in the recent review by Espaillat et al. (2014), together with other results that differ somehow from the ones listed above. In particular, Espaillat et al. (2014) report values of \dot{M}_{acc} for 3 TDs in ρ -Ophiucus which are compatible with the locus of cTTs in the same region and in Taurus on the $\dot{M}_{\text{acc}}-M_d$ plane.

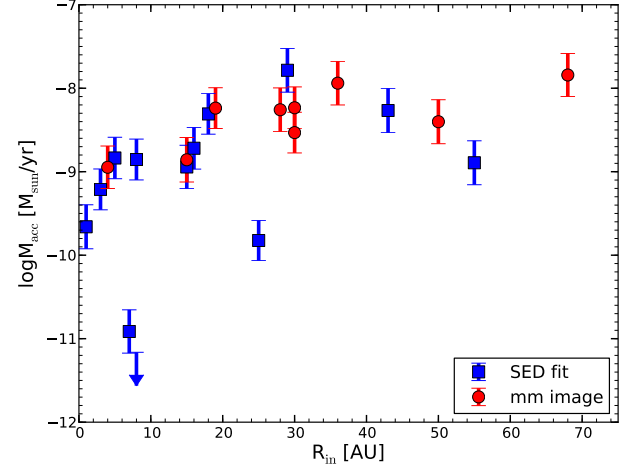


Fig. 8. Logarithm of the mass accretion rate vs inner hole size for our sample. Different symbols are used to distinguish the methods used in the literature to derive the size of the inner hole. *Blue squares* are adopted when this has been derived using IR-SED fitting, while *red circles* when the values are derived from resolved mm-interferometry observations. Downward arrows are upper limits. The two lowest points are, from left to right, CHXR22E and Ser29. The object at $R_{\text{in}}=25$ AU and $\log \dot{M}_{\text{acc}}=-9.8$ is Ser34.

They suggest that results differing from those found in previous works may arise from different sample selection and/or different methods to estimate \dot{M}_{acc} . To avoid this possible methodological bias, we have shown here only the comparison between our sample of TDs and the sample of cTTs in Lupus, which is analyzed in the same way as our objects. We stress here again that our TDs have been selected to be mostly strong accretors, thus our sample selection is not representative of all the TDs and that we do not derive conclusions for the whole TD population. Nevertheless, our results prove that there are TDs that accrete at the same rate of cTTs.

The two main outliers in Fig. 8-9 are the object with an upper limit on L_{acc} , Ser29, and CHXR22E. The lower intensity of accretion for these targets implies that the gas density in the inner disk is substantially depleted with respect to the one of cTTs. These objects do not have any peculiar property reported in the literature. From Fig. 9 we note that in the same range of M_* of these objects there are other TDs with values of \dot{M}_{acc} comparable or even higher than cTTs. Therefore, these objects are not peculiar in their stellar properties. We will discuss in more detail about these objects later after considering their wind and dusty inner disk properties. It is possible that these objects are part of a population of TDs with lower values of \dot{M}_{acc} not included in our sample.

5.2. Wind properties

As discussed in Sect. 4, we have measured the flux of the LVC of the [OI] λ 630 nm line, which is a tracer of winds in YSOs. To determine whether the wind properties of our objects depend on the disk morphology we compare in Fig. 10 the logarithmic luminosity of this line with the values of R_{in} available from the literature. We do not see any clear correlation between these quantities. The luminosity of the LVC of the [OI] λ 630 nm

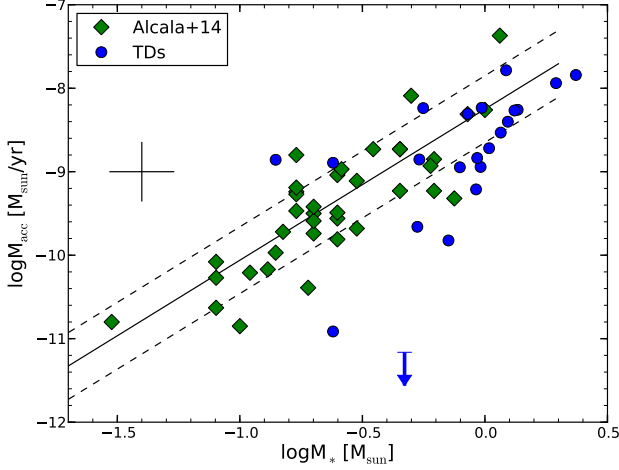


Fig. 9. Logarithm of the mass accretion rate vs logarithm of the stellar mass for our sample of TDs and for a sample of classical T Tauri stars from Alcalá et al. (2014). Our targets are shown as *blue circles*, while data from the literature are reported with *green diamonds*. The lines are the best fit to the data reported in Alcalá et al. (2014) (solid line) and the 0.4 dex spread reported in that study. Downward arrows are upper limits. The two lowest points are, from left to right, CHXR22E and Ser29. Typical errors are shown with the black cross.

line ($L_{\text{[OI]630}}$) appears constant regardless the size of the dust depleted cavity in the disk with values between $\sim 10^{-6}$ and $\sim 10^{-4} L_{\odot}$. This implies that the properties of the wind traced by the [OI] $\lambda 630$ nm line - that can be a disk wind, an accretion-driven wind, or a photoevaporative wind - are similar in most of the TDs in our sample. The question then is where in the disk the wind is originated. With the data in our hands we cannot put any constraint on the emitting region. Analysis of higher-resolution spectra of this line (e.g., Rigliaco et al., 2013) showed that, in cTTs, the emission region can be as close to the star as ~ 0.2 AU, which is well within the dust depleted cavity in all our objects. Models of X-ray photoevaporation (Ercolano & Owen, 2010) predict that the luminosity of this line is insensitive to the size of the inner hole and depend mostly on the EUV and X-ray luminosity (L_X) of the central star. The X-ray photons are responsible for driving the wind in the first place, while the EUV photons heat up the inner region of the wind and excite the [OI] line. In this context, the correlation of L_{acc} with $L_{\text{[OI]}}$ (see discussion in the next paragraph and Fig. 11) could be due to the heating of the wind by the UV photons. Therefore a lack of correlation of $L_{\text{[OI]}}$ with L_X , that is found when comparing our data with the data reported in the literature for L_X (see Table B.1), is not at all surprising, as the emission measure of this line is determined by the UV luminosity, which is instead correlated to L_{acc} . For this reason $L_{\text{[OI]}}$ cannot be used as a quantitative tracer of the photoevaporated wind. Higher resolution spectra and more complete grids of models are needed to better constraint the origin of this line.

It is then important to compare the properties of this line in our TDs and in cTTs to understand whether they are similar in the two classes of objects. As comparison samples we select the objects studied by Rigliaco et al. (2013, and references therein) and those observed with X-Shooter and analyzed by Natta et al. (2014). These two samples are representative of different stellar, accretion, and wind properties of cTTs. In particular, the sam-

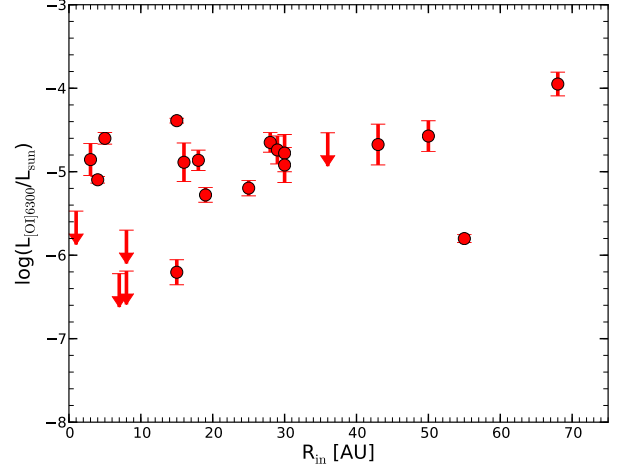


Fig. 10. Logarithmic luminosity of the low-velocity component of the [OI] 630 nm line vs inner hole size for the TDs in our sample. Downward arrows are upper limits.

ple of Rigliaco et al. (2013, and references therein) comprises mostly strong accretors with low to intermediate stellar mass, while Natta et al. (2014) has a sample of low- and very low-mass YSOs with lower accretion rates. Here we compare only the luminosity of the LVC of the [OI] $\lambda 630$ nm line derived in our work and in the comparison samples. The best way to compare these values is to analyze the $L_{\text{[OI]630}}-L_{\text{acc}}$ relation, which is well characterized in the literature (see e.g., Rigliaco et al., 2013, and references therein). This is shown in Fig. 11, where we plot $\log L_{\text{[OI]630}}$ as a function of $\log L_{\text{acc}}$ for our sample of TDs (*red filled circles*) and for the two samples of cTTs (*blue empty circles* for data from Rigliaco et al. 2013 and *green empty circles* for those from Natta et al. 2014). The relation between these two quantities spans over ~ 7 orders of magnitude in both axes with a typical spread of ~ 1 dex for the cTTs, and our objects follow it very well in all the cases. The location of our TDs right in the middle between the two comparison samples reflects the fact that their accretion rates are typical of ~ 0.5 - $1 M_{\odot}$ YSOs, i.e. smaller than those in the sample of Rigliaco et al. (2013) and larger than low-mass YSOs. At the same time, this implies that their wind properties traced by the [OI] $\lambda 630$ nm line scale with the accretion properties in the same fashion as in cTTs. Therefore, the process responsible for the formation of this line should be the same in objects surrounded by dust-rich disks and in TDs.

5.2.1. [NeII] from the literature

To better understand the properties of the winds in our objects we include also data from the literature on the [NeII] $\lambda 12.8 \mu\text{m}$, which is a well known tracer of disk wind. This line has been detected in emission in the mid-infrared spectra of protoplanetary disks using *Spitzer* (e.g. Pascucci et al., 2007; Güdel et al., 2010; Espaillat et al., 2013, and reference therein) or ground-based observations (e.g., Pascucci & Sterzik, 2009; Pascucci et al., 2011; Sacco et al., 2012). This line is of interest to study the inner gaseous disk properties as it traces warm gas ($T \sim 5000$ K) and the effects of extreme ultraviolet (EUV) and X-ray emission from the star on the disk (Glassgold et al., 2007). High-resolution spectroscopic studies constrained the emitting region of this line within 20-40 AU from the central star (Sacco et al.,

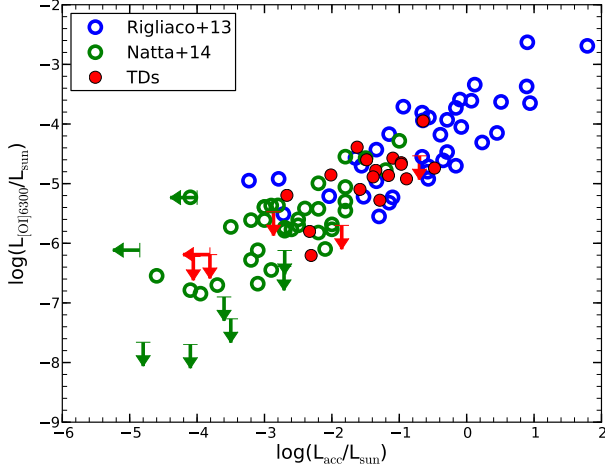


Fig. 11. Logarithmic luminosity of the low-velocity component of the [OI] 630 nm line vs the logarithm of the accretion luminosity of our objects (*red filled symbols*) and for two samples of classical T Tauri stars (*blue empty circles* from Rigliaco et al. 2013, *green empty symbols* from Natta et al. 2014). Downward arrows are upper limits.

2012). High resolution observations of TW Hya, in particular, showed that most ($\geq 80\%$) of the [NeII] emission arises from the region where the disk is still optically thick, but still within ~ 10 AU from the central star (Pascucci et al., 2011).

Among the objects in our sample, 13 have been observed with MIR spectroscopy and all of them have a [NeII] line detection, as we report in Table 6. In all these objects we detected also the [OI] λ 630 nm line, with the only exception being SR21.

5.3. Accretion and wind properties in objects with inner disk emission

Following the analysis described in Sect. 3, we divide the sample in two classes of objects: we refer to objects with no near-infrared color excess as TD, while those with excess are referred to as PTD, as reported in Table 3. The morphological difference between these two classes is the presence of warm dust in the inner region of the disk of PTD, which could be a small ring of dust at few tenths of AU from the star (e.g., Benisty et al., 2010; Espaillat et al., 2010). This difference in the inner disk morphology could be due to different evolutionary stages of these two classes of objects or to different dust depleting mechanisms. Here we compare the accretion and wind properties of the objects in these two classes present in our sample to verify whether we see any difference among these objects.

The comparison of the accretion properties of TDs and PTDs is carried out using the logarithmic $\dot{M}_{\text{acc}}-M_*$ relation, which is shown in Fig. 12. In this figure different symbols are used to plot TDs (*red circles*) and PTDs (*blue squares*). We overplot here the best fit relation from Alcalá et al. (2014) as in Fig. 9 that is used as a reference. We clearly see that there is not a significant difference between the two classes of objects. Similarly to what we discuss in Sect. 5.1, also this result is apparently at odd with previous studies, which showed that PTDs accrete at a lower rate than TDs (e.g., Espaillat et al., 2010; Kim et al., 2013). This implies that the accretion properties in our sample of TDs are independent on the dusty inner disk morphology.

Table 6. Properties of [NeII] $\lambda 12.8\mu\text{m}$ line from the literature

Name	$F_{[\text{NeII}]}_{\text{Hires}}$	FWHM	v_0	$F_{[\text{NeII}]}_{\text{Spitzer}}$	Ref
LkH α 330	0.38 ± 0.19	G10
DM Tau	0.55	G10
LkCa 15	< 0.5	0.28 ± 0.02	S12
GM Aur	1.2 ± 0.06	G10
Sz Cha	1.62 ± 0.20	E13
TW Hya	3.8 ± 0.3	14.6	-6.2	5.9 ± 1.1	P09,G10
CS Cha	2.3 ± 0.2	27	-3.3	3.63 ± 0.07	P09,E13
CHXR22E
Sz18
Sz27	0.63 ± 0.07	E13
Sz45
Sz84
RX J1615	1.4 ± 0.2	20.5	-7.5	2.76 ± 0.46	S12
Oph22
Oph24
SR 21	0.5 ± 0.1	15.1	-8.3	< 3.0	S12,G10
ISO-Oph196
DoAr 44	< 0.3	0.68 ± 0.33	S12,G10
Ser29
Ser34
RX J1842.9	< 0.2	0.43 ± 0.13	S12,G10
RX J1852.3	0.72 ± 0.04	G10

References. P11: Pascucci et al. (2011); P09: Pascucci & Sterzik (2009); S12: Sacco et al. (2012); E13: Espaillat et al. (2013); G10: Güdel et al. (2010)

Notes. Fluxes are reported in units of 10^{-14} erg s $^{-1}$ cm $^{-2}$; v_0 and FWHM in units of km/s.

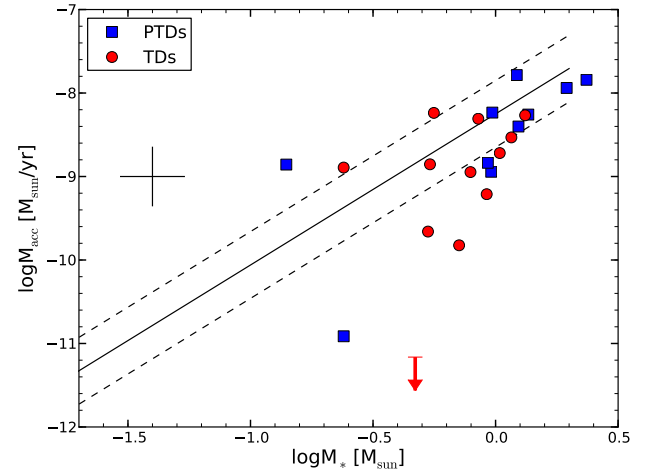


Fig. 12. Logarithm of the mass accretion rate vs logarithm of the stellar mass of our sample. Different symbols are used to distinguish objects with inner disk emission (*blue squares*) from TDs with no IR-excess (*red circles*).

We proceed with this analysis by comparing in Fig. 13 the logarithmic relation between L_{acc} and $L_{[\text{OI}]630}$ for our sample, using different symbols for TDs (*red circles*) and for PTDs (*blue squares*) to see whether wind properties depend on the inner disk properties. Also in this case there is no correlation between the position on the plot and the inner disk morphology. The wind properties traced by the [OI] λ 630 nm line are thus independent of the presence of dust in the innermost region of the disk.

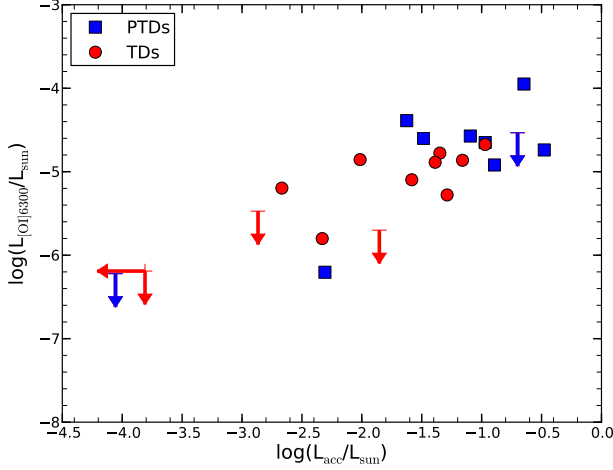


Fig. 13. Logarithmic luminosity of the low-velocity component of the [OI] 630 nm line vs the logarithm of the accretion luminosity of our objects. Symbols and colors are the same as in Fig. 12.

5.4. Constraint on the gas content of the inner disk

Here we present additional constraint on the region in the inner disk where gas is present and on its properties. From observations obtained in the literature we have measurement on the emission from CO from the inner part of the disk, which we discuss in the next subsection. Then, using the information on the accretion properties of our targets we derive the extent of the gas-rich inner disk, which extends down to the magnetospheric radius (R_m) at few stellar radii. We then also derive the density of gas in the inner disk needed to sustain the observed \dot{M}_{acc} if the disk is assumed in “steady-state”. We also discuss possibilities to explain the observed \dot{M}_{acc} , and thus for a gas-rich inner disk, allowing for a significant gas depletion in the disk gaps. Finally, we give a complete view of the gas content of the inner disk adding to these informations also the wind properties of our TDs.

5.4.1. CO emission from the literature

The fundamental ($\Delta v = 1$) rovibrational line of CO at $4.7 \mu m$ is an important diagnostic to constraint the presence of gas in the inner region of TDs. This is sensitive to gas temperatures of 100-1000 K, which correspond to radii of 0.1-10 AU in typical protoplanetary disks around solar-mass stars YSOs, assuming that it originates in the so-called “warm molecular layer” of the disk. Study of high-resolution spectra of this line have determined with high precision its emitting region within the disk (Najita et al., 2003; Salyk et al., 2007; Pontoppidan et al., 2008; Salyk et al., 2009; Pontoppidan et al., 2011). These studies observed 7 objects included in this work, and detected the line in all of them besides DM Tau. We report in Table 7 the inner radius of the CO emission in the disks ($R_{in,CO}$) derived from the studies in the literature. Additional studies on three other objects of our sample have detected this line in RX J1842.9, while non-detection are obtained in the spectra of Sz Cha and RX J1852.3 (A. Carmona, personal communication). Seven out of the ten objects where this line has been studied are classified as PTD, so this emission could arise from the dusty inner disk. However, we also see that CO can be emitted in the dust-depleted inner disk

Table 7. Properties of CO fundamental transition from the literature.

Name	$R_{in,CO}$ [AU]	Ref
LkH α 330	4 ± 1	P11
DM Tau	... ^a	S09
LkCa 15	0.093	N03
GM Aur	0.5 ± 0.2	S09
Sz Cha	... ^c	...
TW Hya	0.11 ± 0.07	P08
CS Cha
CHXR22E
Sz18
Sz27
Sz45
Sz84
RX J1615
Oph22
Oph24
SR 21	7.6 ± 0.4	P08
ISO-Oph196
DoAr44	0.4 ± 0.1	S09
Ser29
Ser34
RX J1842.9	... ^b	...
RX J1852.3	... ^c	...

References. S09: Salyk et al. (2009); N03: Najita et al. (2003); P08: Pontoppidan et al. (2008); P11: Pontoppidan et al. (2011). ^a Non detection. Personal communications from A. Carmona: ^b detection of CO line, ^c non detection of CO line.

of some TDs, such as TW Hya or RX J1852.3. A possible explanation for the emission of CO in the case of TW Hya is local warming due to the presence of a companion orbiting in the gap (Arnold et al., 2012). In any case, the detection of CO emission in the aforementioned objects confirms that their inner disk is gas-rich, confirming the results obtained by detecting ongoing accretion in the same targets.

5.4.2. Magnetospheric radius

In the context of magnetospheric accretion models (e.g., Hartmann et al., 1998) the position in the disk from where the gas is accreted onto the star is determined by R_m . This is the radius where the external torque due to star-disk magnetic interaction dominates over the viscous torque. Following Armitage (2010), this can be derived by equating the expressions representing the two timescales involved in this process, namely the magnetospheric accretion timescale:

$$t_m \sim 2\pi \frac{\Sigma \sqrt{GM_* r}}{B_z^s B_\phi^s r}, \quad (1)$$

where r is the radial distance in the disk from the central star, B is the magnetic field, the superscript s stands for magnetic field evaluated at the disk surface, and Σ is the surface density of the gas, and the viscous timescales:

$$t_\nu \sim \frac{r^2}{\nu}, \quad (2)$$

where ν is the disk viscosity. We assume the steady-state disk relation for the viscosity:

$$\nu \Sigma = \frac{\dot{M}_{acc}}{3\pi}, \quad (3)$$

that implies a constant \dot{M}_{acc} in the disk, and we consider the simple case where the stellar magnetic field is bipolar and oriented in the same direction as the rotation axis of the star. With these assumptions, we derive the usual relation for R_m (e.g. Hartmann, 2009):

$$R_m \sim \left(\frac{3B_*^2 R_*^6}{2\dot{M}_{\text{acc}} \sqrt{GM_*}} \right)^{2/7}. \quad (4)$$

It is important to note that this quantity depends weakly on \dot{M}_{acc} , M_* , and to B_* . The stronger dependence is on R_* . Using this relation we are able to derive the values of R_m for all the accreting TDs in our sample using the values of \dot{M}_{acc} ², M_* , and R_* derived in Sect. 3, and assuming a typical value for the magnetic field of the star $B_* \sim 1$ kG (e.g. Johnstone et al., 2014). The effect of the arbitrary choice of the value of B_* is the prominent source of uncertainty in our estimate of R_m . We have to adopt a typical value for B_* since only for two targets in our sample this quantity has been measured. This is the case of TW Hya and GM Aur, where B_* is 1.76 kG and 1 kG, respectively (Johns-Krull, 2007). By varying the values of B_* from 2 kG to 0.5 kG we estimate a relative uncertainty on R_m of less than 0.5. This is then the assumed uncertainty of our estimate.

The values of R_m we have derived are reported in Table 8. In all the objects $R_m > 5R_*$, in accordance with magnetospheric accretion models. This radius is always located at a distance from the central star much smaller than R_{in} . The detection of ongoing accretion implies that gas is present in the disk at this distance from the star. The gas density in the region of the disk at radii $\sim R_m$ can be estimated as we explain in the next subsection.

5.4.3. Density of gas in the inner disk

Assuming steady-state disk condition the surface density of the gas is related to the accretion disk viscosity and \dot{M}_{acc} by the relation reported in Eq. (3). We describe the viscosity using the α viscosity prescription ($\nu = \alpha c_s H$, Shakura & Sunyaev, 1973) and we assume that the disk is vertically isothermal, so that $H = c_s / \Omega(r)$, where $c_s = (kT / \mu m_p)^{1/2}$ is the sound speed, $\mu = 2.3$ is the mean molecular weight, m_p is the mass of the proton, and $\Omega = (GM_* / r^3)^{1/2}$ is the angular velocity of the disk. We then derive the following relation for the surface density of the gas in the disk:

$$\Sigma(r) \sim \frac{2m_p}{3\pi\alpha k_B T(r)} \dot{M}_{\text{acc}} \sqrt{\frac{GM_*}{r^3}}. \quad (5)$$

We estimate the surface density of the gas at a distance of 1 AU from the central star ($\Sigma_{1\text{AU}}$). This radius is chosen because it is much larger than R_m but still within R_{in} for all our targets. Assuming $\alpha = 10^{-2}$ and $T(1\text{AU}) = 200$ K (representative value derived from Andrews & Williams, 2007), we derive the values of $\Sigma_{1\text{AU}}$ from the central star reported in Table 8. These values vary from few g cm^{-2} to $\sim 4 \times 10^2 \text{ g cm}^{-2}$ for our objects, and represent the expected densities of gas in the disk inner region needed to sustain the observed accretion rates assuming steady

² The values of \dot{M}_{acc} derived previously have been obtained assuming $R_m = 5 R_*$. This is the usual assumption made in the literature, thus this value is the appropriate one to derive \dot{M}_{acc} consistently to previous analyses. The same values of \dot{M}_{acc} can be adopted here because of the weak dependence of R_m on \dot{M}_{acc} ($R_m \propto \dot{M}_{\text{acc}}^{-2/7}$). By re-deriving \dot{M}_{acc} using the newly determined R_m we obtain values of \dot{M}_{acc} with a typical difference of ~ 0.05 dex and always smaller than 0.1 dex. This translates in relative uncertainties on the value of R_m of less than 0.06.

Table 8. Derived properties of the gas

Name	R_m [R_*]	R_m [AU]	$\Sigma_{1\text{AU}}$ [g cm^{-2}]
LkH α 330	10.05	0.175	411.36
DM Tau	7.94	0.058	106.87
LkCa 15	8.35	0.059	82.81
GM Aur	7.46	0.061	174.28
Sz Cha	5.54	0.039	337.56
TW Hya	8.37	0.033	19.17
CS Cha	8.07	0.062	116.45
CHXR22E	35.18	0.134	0.12
Sz18	10.88	0.068	23.91
Sz27	9.73	0.052	24.61
Sz45	7.50	0.053	118.54
Sz84	14.55	0.113	15.01
RX J1615	9.49	0.084	92.24
Oph22	24.22	0.240	4.63
Oph24	13.13	0.089	15.08
SR 21	8.97	0.117	299.26
ISO–Oph196	11.51	0.054	9.45
DoAr 44	6.28	0.032	102.45
Ser29
Ser34	18.61	0.106	2.95
RX J1842.9	8.88	0.043	25.22
RX J1852.3	9.08	0.051	34.91

state viscous inner disk. Another possibility is that the density of the gas in the cavity is lower than the one derived here if the radial inflow of gas is at high velocity, approaching free-fall (Rosenfeld et al., 2014). Finally, episodic events that replenish the gas content of the inner disk from the outer disk could also possibly explain our observed \dot{M}_{acc} with a significantly gas depleted hole for most of the TD lifetime.

5.5. Discussion on the gas content of the inner disk

We now want to put together all the information collected from our spectra and from the literature on the objects in our sample to understand what is the morphology of their gaseous inner disk. The discussion is divided between accreting and non-accreting objects. All the objects analyzed in this work besides Ser 29 have accretion detected with our method. Also CHXR22E has a measured value of \dot{M}_{acc} lower than other objects with similar stellar properties, as we pointed out when discussing the result of Fig. 9. We discuss these two objects in Sect. 5.5.2, while the other 20 accreting objects are discussed in the next subsection.

5.5.1. Accreting transitional disks

As discussed in the introduction, the detection of measurable accretion rates in young stellar objects implies that the innermost region of the disk is gas rich. This is the case for our accreting TDs, and we derived in Sect. 5.4.2 and 5.4.3 the inner boundary of the gaseous disk in these objects and the densities of the gas in the inner disk needed to sustain the observed accretion rates assuming a steady-state viscous disk. We constrain with our analysis that gas is present in these disks in regions as close to the star as $\sim 0.03 - 0.3$ AU, that are the values of R_m . The evidence of gas presence in this region is confirmed in 17 of the 20 accreting TDs with the detection of the [OI] λ 630 nm line in their spectra, which is originated as close as ~ 0.2 AU from the star. At similar disk radii ($\sim 0.1-0.5$ AU) the CO emission is detected in 4 objects (LkCa15, GM Aur, TW Hya, and DoAr 44, see Table 7), confirming the presence of gas in their inner disk.

For TW Hya this region is known to be strongly dust-depleted. On the other hand, it is plausible that the CO emission arises from the dusty inner disk in the other three objects, known to be PTDs. To these objects we should add RX J1842.9 where the CO line is also detected, but no analysis has yet been carried out to determine the distance to the star of the region emitting this line. For LkHa330 and SR21 the emission of the CO line arises from larger radii ($R_{\text{CO}} \geq 4$ AU) due to the higher temperature of the disk related to the larger L_* of these objects compared to the rest of the sample. Finally, in 13 of the 20 accreting TDs we could find a detection of the [NeII] in the literature. This line is also originated in a wind coming from a gas rich region of the disk inside a distance from the central star of ~ 20 -40 AU. In only 9 of the 20 accreting TDs we found evidence of infrared excess, a signature of the presence of a dusty inner disk.

The picture of these accreting TDs coming from our analysis is then the following. These are objects with a gas rich disk well within the observed R_{in} , i.e. at the inner disk edge. Given that we do not find any correlation between the dust-depleted hole and the accretion or wind properties, and that we see both accreting TDs with dusty inner disks and without, the model needed to explain the formation of the dust-depleted inner region should leave almost unaltered the gas properties of the innermost region. From the point of view of the gas content of the inner disk there is no observable difference between accreting TDs and cTTs.

5.5.2. Non-accreting transitional disks

The two objects we discuss here (Ser 29 and CHXR22E) have a gas-depleted inner region of the disk. The non-detection of accretion signatures in these objects or the very low detected \dot{M}_{acc} of CHXR22E imply that the density of the gas in this region of the disk is smaller in these objects by at least one order of magnitude than in any other accreting object. This is clearly seen in the value of $\Sigma_{\text{IAU}} = 0.1 \text{ g cm}^{-2}$ reported for CHXR22E in Table 8, smaller by a factor ~ 30 -40 than the one computed for Oph 22 and Ser 34, that have similar stellar properties. With the addition of the non-detection of the [OI] λ 630 nm in the spectra of both objects we conclude that the region around ~ 0.1 -0.3 AU is significantly gas-depleted in these non-accreting TDs. No further information on the gas content of the inner disk of Ser 29 and CHXR22E are available. These two targets should be observed in the future with the aim of detecting [NeII] and/or CO emission in the inner parts of these objects, in order to constraint the inner boundary of the gas-rich disk.

6. Conclusions

In this work we analyzed a sample of 22 X-Shooter spectra of TDs. This sample comprises objects with different outer disk morphologies, in particular with values of R_{in} ranging from ~ 1 AU to ~ 70 AU, and includes mainly TDs with previous accretion rate estimates. This sample cannot provide a conclusive statistical result on the general properties of the TD class, but it is a good benchmark to study with an highly reliable method these objects. We used a multi-component fitting method to derive simultaneously the SpT, A_V , and L_{acc} of the objects fitting our broad-band spectra. At the same time we derived from the same spectra the intensity of the [OI] λ 630 nm line. From the analysis of the results we derived the following conclusions:

- The dependence of the accretion properties of our sample of strongly accreting TDs with the size of the dust-depleted cavity (R_{in}) is small, in particular there is no evidence for increasing \dot{M}_{acc} with R_{in} at values of $R_{\text{in}} \gtrsim 20 - 30$ AU;

- There are strongly accreting TDs, like the majority of the objects in our sample, whose accretion properties are consistent with those reported in the literature for cTTs;

- The wind properties of the TDs analyzed here have no dependence with the size of the dust-depleted cavity (R_{in}) and are consistent with the wind properties of cTTs;

- There are no differences in the accretion and wind properties between the objects in our sample with inner disk emission (PTD) or without (TD);

- Strongly accreting TDs such as those analyzed here are gas-rich down to distances from the central star as small as ~ 0.03 -0.3 AU as can be obtained from the derivation of the values of R_m , from the detection of the [OI] λ 630 nm line, and from the detection of the CO and [NeII] lines. This distance is always smaller than the values of R_{in} reported in the literature for these objects, meaning that there is a gaseous inner disk much closer to the star than the dusty one;

- Non-accreting TDs have gas depleted inner disks. The gaseous disk is significantly depleted of gas at a distance from the star of at least ~ 0.03 -0.3 AU. Also for these objects the inner extent of gas and dust in the disk are uncoupled;

- The process needed to explain the formation of TDs should act differently on the gas and the dust components of the disk.

Future studies aimed at understanding the process responsible for the formation of the dust depleted cavity in TDs should aim at:

- conducting a similar analysis on a larger and more complete sample of TDs, including a larger amount of objects known to accrete at lower rates than those included in this work;

- determining the process responsible for the formation of the forbidden lines - photoevaporation, disk wind, or other possibilities - from the analysis of high-resolution and high-signal to noise forbidden lines and the comparison with theoretical models covering more completely the parameter space of stellar properties;

- determining the extent of the region emitting the [OI] and [NeII] line and the density of gas in this region in order to put stronger constraint on the distance from the central star at which gas is present;

- studying the CO line with high-resolution spectroscopy in non-accreting TDs to verify the decoupling of the gas-rich and dust-rich disk in these objects.

Acknowledgements. We thank the ESO staff in Paranal for carrying out the observations in Service mode. We thank J. Alcalá and the “JETS and Disk at Inaf” (JEDI) team for providing the reduced spectrum of Sz84. We thank A. Carmona for sharing the information on the CO line detection. C.F.M. acknowledges the PhD fellowship of the International Max-Planck-Research School.

References

- Alcalá, J. M., Natta, A., Manara, C. F., et al. 2014, *A&A*, 561, A2
- Alexander, R., Pascucci, I., Andrews, S., Armitage, P., & Cieza, L. 2014, arXiv:1311.1819
- Andrews, S. M., & Williams, J. P. 2007, *ApJ*, 659, 705
- Andrews, S. M., Wilner, D. J., Hughes, A. M., Qi, C., & Dullemond, C. P. 2009, *ApJ*, 700, 1502
- Andrews, S. M., Wilner, D. J., Espaillat, C., et al. 2011, *ApJ*, 732, 42
- Armitage, P. J. 2010, *Astrophysics of Planet Formation*, by Philip J. Armitage, pp. 294. ISBN 978-0-521-88745-8 (hardback). Cambridge, UK: Cambridge University Press, 2010.,
- Arnold, T. J., Eisner, J. A., Monnier, J. D., & Tuthill, P. 2012, *ApJ*, 750, 119
- Baraffe, I., Chabrier, G., Allard, F., & Hauschildt, P. H. 1998, *A&A*, 337, 403
- Benisty, M., Tatulli, E., Ménard, F., & Swain, M. R. 2010, *A&A*, 511, A75
- Birnstiel, T., Andrews, S. M., & Ercolano, B. 2012, *A&A*, 544, A79
- Brown, J. M., Blake, G. A., Dullemond, C. P., et al. 2007, *ApJ*, 664, L107
- Brown, J. M., Blake, G. A., Qi, C., Dullemond, C. P., & Wilner, D. J. 2008, *ApJ*, 675, L109

- Brown, J. M., Blake, G. A., Qi, C., et al. 2009, *ApJ*, 704, 496
- Calvet, N., D'Alessio, P., Hartmann, L., et al. 2002, *ApJ*, 568, 1008
- Calvet, N., Muzerolle, J., Briceño, C., et al. 2004, *AJ*, 128, 1294
- Calvet, N., D'Alessio, P., Watson, D. M., et al. 2005, *ApJ*, 630, L185
- Cardelli, J. A., Clayton, G. C., & Mathis, J. S. 1989, *ApJ*, 345, 245
- Chapman, N. L., Mundy, L. G., Lai, S.-P., & Evans, N. J., II 2009, *ApJ*, 690, 496
- Cieza, L., Padgett, D. L., Stapelfeldt, K. R., et al. 2007, *ApJ*, 667, 308
- Costigan, G., Scholz, A., Stelzer, B., et al. 2012, *MNRAS*, 427, 1344
- Currie, T., & Sicilia-Aguilar, A. 2011, *ApJ*, 732, 24
- Dahm, S. E. 2008, *AJ*, 136, 521
- D'Antona, F., & Mazzitelli, I. 1994, *ApJS*, 90, 467
- Ercolano, B., & Owen, J. E. 2010, *MNRAS*, 406, 1553
- Ercolano, B., Mayr, D., Owen, J. E., Rosotti, G., & Manara, C. F. 2014, *MNRAS*, 178
- Españillat, C., D'Alessio, P., Hernández, J., et al. 2010, *ApJ*, 717, 441
- Españillat, C., Ingleby, L., Hernández, J., et al. 2012, *ApJ*, 747, 103
- Españillat, C., Ingleby, L., Furlan, E., et al. 2013, *ApJ*, 762, 62
- Españillat, C., Muzerolle, J., Najita, J., et al. 2014, *arXiv:1402.7103*
- Forbrich, J., & Preibisch, T. 2007, *A&A*, 475, 959
- Glassgold, A. E., Najita, J. R., & Igea, J. 2007, *ApJ*, 656, 515
- Grosso, N., Montmerle, T., Bontemps, S., André, P., & Feigelson, E. D. 2000, *A&A*, 359, 113
- Güdel, M., Lahuis, F., Briggs, K. R., et al. 2010, *A&A*, 519, A113
- Guenther, E. W., Esposito, M., Mundt, R., et al. 2007, *A&A*, 467, 1147
- Hartigan, P., Edwards, S., & Ghandour, L. 1995, *ApJ*, 452, 736
- Hartmann, L., Calvet, N., Gullbring, E., & D'Alessio, P. 1998, *ApJ*, 495, 385
- Hartmann, L. 2009, *Accretion Processes in Star Formation: Second Edition*, by Lee Hartmann. ISBN 978-0-521-53199-3. Published by Cambridge University Press, Cambridge, UK, 2009.,
- Herczeg, G. J., & Hillenbrand, L. A. 2008, *ApJ*, 681, 594
- Hughes, A. M., Wilner, D. J., Calvet, N., et al. 2007, *ApJ*, 664, 536
- Hughes, A. M., Wilner, D. J., Qi, C., & Hogerheijde, M. R. 2008, *ApJ*, 678, 1119
- Hughes, A. M., Andrews, S. M., Wilner, D. J., et al. 2010, *AJ*, 140, 887
- Ingleby, L., Calvet, N., Bergin, E., et al. 2009, *ApJ*, 703, L137
- Ingleby, L., Calvet, N., Herczeg, G., et al. 2013, *ApJ*, 767, 112
- Johns-Krull, C. M. 2007, *ApJ*, 664, 975
- Johnstone, C. P., Jardine, M., Gregory, S. G., Donati, J.-F., & Hussain, G. 2014, *MNRAS*, 437, 3202
- Kenyon, S. J., & Hartmann, L. 1995, *ApJS*, 101, 117
- Kim, K. H., Watson, D. M., Manoj, P., et al. 2009, *ApJ*, 700, 1017
- Kim, K. H., Watson, D. M., Manoj, P., et al. 2013, *ApJ*, 769, 149
- König, B., Neuhauser, R., & Stelzer, B. 2001, *A&A*, 369, 971
- Krautter, J., Wichmann, R., Schmitt, J. H. M. M., et al. 1997, *A&AS*, 123, 329
- Lada, C. J., Muench, A. A., Luhman, K. L., et al. 2006, *AJ*, 131, 1574
- Luhman, K. L., Rieke, G. H., Lada, C. J., & Lada, E. A. 1998, *ApJ*, 508, 347
- Luhman, K. L., Stauffer, J. R., Muench, A. A., et al. 2003, *ApJ*, 593, 1093
- Luhman, K. L. 2008, *Handbook of Star Forming Regions, Volume II*, 169
- Luhman, K. L., Allen, P. R., Españillat, C., Hartmann, L., & Calvet, N. 2010, *ApJS*, 189, 353
- Manara, C. F., Robberto, M., Da Rio, N., et al. 2012, *ApJ*, 755, 154
- Manara, C. F., Testi, L., Rigliaco, E., et al. 2013a, *A&A*, 551, A107
- Manara, C. F., Beccari, G., Da Rio, N., et al. 2013b, *A&A*, 558, A114
- Manoj, P., Kim, K. H., Furlan, E., et al. 2011, *ApJS*, 193, 11
- Matrà, L., Merín, B., Alves de Oliveira, C., et al. 2012, *A&A*, 548, A111
- McClure, M. 2009, *ApJ*, 693, L81
- Merín, B., Brown, J. M., Oliveira, I., et al. 2010, *ApJ*, 718, 1200
- Modigliani, A., Goldoni, P., Royer, F., et al. 2010, *Proc. SPIE*, 7737
- Montmerle, T., Koch-Miramond, L., Falgarone, E., & Grindlay, J. E. 1983, *ApJ*, 269, 182
- Muzerolle, J., Hillenbrand, L., Calvet, N., Briceño, C., & Hartmann, L. 2003, *ApJ*, 592, 266
- Muzerolle, J., Allen, L. E., Megeath, S. T., Hernández, J., & Gutermuth, R. A. 2010, *ApJ*, 708, 1107
- Najita, J., Carr, J. S., & Mathieu, R. D. 2003, *ApJ*, 589, 931
- Najita, J. R., Strom, S. E., & Muzerolle, J. 2007, *MNRAS*, 378, 369
- Natta, A., Testi, L., & Randich, S. 2006, *A&A*, 452, 245
- Natta, A., Testi, L., et al. *A&A*, in prep.
- Neuhauser, R., Sterzik, M. F., Schmitt, J. H. M. M., Wichmann, R., & Krautter, J. 1995, *A&A*, 297, 391
- Neuhauser, R., Walter, F. M., Covino, E., et al. 2000, *A&AS*, 146, 323
- Owen, J. E., Ercolano, B., & Clarke, C. J. 2011, *MNRAS*, 412, 13
- Owen, J. E., Clarke, C. J., & Ercolano, B. 2012, *MNRAS*, 422, 1880
- Pascucci, I., Hollenbach, D., Najita, J., et al. 2007, *ApJ*, 663, 383
- Pascucci, I., & Sterzik, M. 2009, *ApJ*, 702, 724
- Pascucci, I., Sterzik, M., Alexander, R. D., et al. 2011, *ApJ*, 736, 13
- Peterson, D. E., Caratti o Garatti, A., Bourke, T. L., et al. 2011, *ApJS*, 194, 43
- Piétu, V., Dutrey, A., Guilloteau, S., Chapillon, E., & Pety, J. 2006, *A&A*, 460, L43
- Pinilla, P., Benisty, M., & Birnstiel, T. 2012, *A&A*, 545, A81
- Pontoppidan, K. M., Blake, G. A., van Dishoeck, E. F., et al. 2008, *ApJ*, 684, 1323
- Pontoppidan, K. M., Blake, G. A., & Smette, A. 2011, *ApJ*, 733, 84
- Rigliaco, E., Natta, A., Randich, S., Testi, L., & Biazzo, K. 2011, *A&A*, 525, A47
- Rigliaco, E., Natta, A., Testi, L., et al. 2012, *A&A*, 548, A56
- Rigliaco, E., Pascucci, I., Gorti, U., Edwards, S., & Hollenbach, D. 2013, *ApJ*, 772, 60
- Rodgers-Lee, D., Scholz, A., Natta, A., & Ray, T. 2014, *arXiv:1405.3833*
- Rosenfeld, K. A., Chiang, E., & Andrews, S. M. 2014, *ApJ*, 782, 62
- Rosotti, G. P., Ercolano, B., Owen, J. E., & Armitage, P. J. 2013, *MNRAS*, 430, 1392
- Sacco, G. G., Flaccomio, E., Pascucci, I., et al. 2012, *ApJ*, 747, 142
- Salyk, C., Blake, G. A., Boogert, A. C. A., & Brown, J. M. 2007, *ApJ*, 655, L105
- Salyk, C., Blake, G. A., Boogert, A. C. A., & Brown, J. M. 2009, *ApJ*, 699, 330
- Shakura, N. I., & Sunyaev, R. A. 1973, *A&A*, 24, 337
- Sicilia-Aguilar, A., Henning, T., & Hartmann, L. W. 2010, *ApJ*, 710, 597
- Vernet, J., Dekker, H., D'Odorico, S., et al. 2011, *A&A*, 536, A105
- White, N. E., Giommi, P., & Angelini, L. 2000, *VizieR Online Data Catalog*, 9031, 0
- White, R. J., & Ghez, A. M. 2001, *ApJ*, 556, 265
- Zhu, Z., Nelson, R. P., Hartmann, L., Españillat, C., & Calvet, N. 2011, *ApJ*, 729, 47

Appendix A: Comments on individual objects

A.1. Sample properties

LkCa 15: this object has been resolved with 880 μm interferometric observations by Andrews et al. (2011), and its cavity was previously resolved at 1.3 mm by Piétu et al. (2006). The modelling of this target carried out by Andrews et al. (2011) has a discrepancy with the observed 880 μm flux inside the cavity probably due to dust emission.

Sz Cha: we observed only the primary component of this wide binary system with separation $5''.122$. The companion of this object is not a confirmed member of the Cha I association (Luhman, 2008).

CS Cha: Guenther et al. (2007) classified this objects as a spectroscopic binary with a period of more than 2482 days. The minimum mass of the companion is $0.1 M_{\odot}$.

Sz 84: It is under debate whether this object should be classified as TD. Merín et al. (2010), who classified it as a TD in first place, derived $R_{\text{in}} = 55 \pm 5$ AU, but they pointed out that the classification was rather uncertain due to possible extended emission contamination. Also Matrà et al. (2012) suggest that this classification is dubious. They point out that this object has no 10 μm silicate feature in the spectrum, which is a typical feature in the spectra of TDs. Then, they report that it has a SED very similar to the one of T54, which they propose is not a TD due to extended emission in the *Herschel* images.

RX J1615-3255: different distances for this object are reported in the literature. Merín et al. (2010) consider this object to be located in the ρ -Ophiuci cloud, thus at $d=125$ pc. Andrews et al. (2011), instead, adopt a distance to this object of 185 pc because they assume it is located in the Lupus cloud. This location is then adopted also by Sacco et al. (2012), but they use a distance of 150 pc for the object. We decide to adopt the distance of 185 pc used by Andrews et al. (2011) for consistency with the values of R_{in} derived in that work. We then correct the value of R_{in} derived in Merín et al. (2010) to the distance adopted here. This is the value of $R_{\text{in,SED}}$ reported in Table B.1.

SR21: this object is known to be a wide binary with a separation of $\sim 6''.4 \sim 770$ AU. We observed only the primary component of the system, which is the one observed by Andrews et al. (2011). Regarding the dust emission of this object, Andrews et al. (2011) report a poor matching of the observations which may indicate

that a small amount of \sim mm-sized dust particles is present in the cavity.

ISO-Oph196: the inner dust depleted cavity has been barely resolved with SMA by Andrews et al. (2011). Looking at the SED of this object there is no signature of dust depletion, i.e. there is no dip in the MIR SED. This suggests that the dust is not strongly depleted in the inner disk of this object.

Appendix B: Additional literature data

We report in Table B.1 additional data collected in the literature on our targets. These data have not been used in this work but are useful for further analysis. The spectral type and \dot{M}_{acc} reported here have not been used in our analysis.

Table B.1. Stellar and disk parameters available in the literature

Name	Spectral type	\dot{M}_{acc} [$10^{-8} M_{\odot}/\text{yr}$]	$R_{\text{gap,in,SED}}$ [AU]	$R_{\text{in,SED}}$ [AU]	$R_{\text{in,mm}}$ [AU]	i [$^{\circ}$]	$\log L_X$ [erg/s]	Disk Type	Ref
LkH α 330	G3	0.20	0.8	50	68	35	1,12,22,26
DM Tau	M1	0.60	...	3	19	35	30.30	TD	1,10,20,21,28
LkCa15	K3	0.30	4	48	50	49	<29.6	PTD	1,15,16,21,24
GM Aur	K5	1.00	1	24	28	55	30.20	TD	6,9,10,20,21,28
SZ Cha	K0	0.24	...	29	29.90	PTD	16,17,21,25
TW Hya	K7	0.20	...	4	4	4	30.32	...	10,14,23,27
CS Cha	K6	0.53	...	43	...	45	30.56	TD	10,16,24,25,30
CHXR22E	M3.5	7	29.41	TD	16,19
Sz18	M3	1.5e-10	...	8	TD	16,19
Sz27	M0	1.2e-9	...	15	29.76 ^a	PTD	16,19
Sz45	M0.5	7.6e-10	...	18	WTD	16,19
Sz84	M5.5	1.00	...	55	8
RX J1615	K5	0.04	...	3 ^b	30	41	30.40	...	1,2,8
Oph22	M2	1	8
Oph24	M0.5	1.00	...	3	8
SR 21	G3	<0.1	0.45	18	36	22	30.00	...	1,3,4,5,18,26
ISO-Oph 196	M4	0.20	15	28	1,18
DoAr 44	K3	0.90	...	27	30	35	29.9	PTD	1,13,29
Ser29	M0	30.00	...	8	8
Ser34	M0	0.25	...	25	8
RX J1842.9	K2	0.10	...	5	30.34	...	6,7,19
RX J1852.3	K3	0.05	...	16	30.41	...	6,7,19

References. (1) Andrews et al. (2011), (2) Krautter et al. (1997), (3) Brown et al. (2009), (4) Andrews et al. (2009), (5) Grosso et al. (2000), (6) Hughes et al. (2010), (7) Neuhäuser et al. (2000), (8) Merín et al. (2010), (9) Hughes et al. (2008), (10) Güdel et al. (2010), (11) König et al. (2001), (12) Brown et al. (2008), (13) Montmerle et al. (1983), (14) Hughes et al. (2007), (15) Neuhäuser et al. (1995), (16) Kim et al. (2009), (17) White et al. (2000), (18) Natta et al. (2006), (19) Pascucci et al. (2007), (20) Ingleby et al. (2009), (21) Espaillat et al. (2010), (22) Salyk et al. (2009), (23) Herczeg & Hillenbrand (2008), (24) Ingleby et al. (2013), (25) Espaillat et al. (2013), (26) Brown et al. (2007), (27) Calvet et al. (2002), (28) Calvet et al. (2005), (29) Kim et al. (2013), (30) Pascucci & Sterzik (2009) — $R_{\text{gap,in,SED}}$ is the inner radius of the gap in PTDs obtained from MIR SED fitting, whereas R_{in} is the inner radius of the dusty outer disk, i.e. the outer radius of the gap in PTDs and of the hole in TDs. ^a Highly uncertain parameter. ^b Value corrected for the different distance as explained in Appendix A.1.